communications earth & environment

Article

A Nature Portfolio journal

https://doi.org/10.1038/s43247-025-02817-w

Energetic convergence drives metabolic adaptation in lirima chilean high-altitude hydrothermal system

Pablo Paquis[1,2,3], Coral Pardo-Esté[1], Joseline Tapia[2,4,5], July Z. Florez[1,6], Vilma Pérez[7,8], Verónica Molina[6,9], Marcela Cornejo-D'Ottone[10], Pablo A. Pérez[1], Chris Harrod[11,12], Wade H. Jeffrey[13], Sergio Calabrese[3,14], Paola Quatrini[3], Franco Tassi[15,16] & Martha B. Hengst[1]

High-altitude hydrothermal systems provide laboratories for understanding microbial adaptation to extreme conditions. Here we investigated thermodynamic controls on metabolic transitions in Lirima hydrothermal system (Chile, 4000 meters above sea level) calculating affinities of competing carbon and sulfur reactions across pools (53–75 °C). Through geochemistry, numerical thermodynamic modeling, and stable isotope analysis, we identify Energetic Convergence Nodes where chemical affinities of competing pathways become equal. Calculations reveal hydrogenotrophic and carboxydotrophic methanogenesis converge with sulfate reduction at 63–64 °C. This corresponds with responses: carbon isotopes shift from −17.2‰ to −27.7‰, sulfur isotopes from −20.5‰ to −9.1‰, and carbon-to-sulfur ratios drop from ~10 to <1, indicating transition from carbon to sulfur-dominated metabolism. Microbial activity collapses at this temperature, while metagenomics validates both pathways. Independent analysis confirms convergence at 63–64 °C, establishing Energetic Convergence Nodes as predictive frameworks for metabolic boundaries with applications for early Earth biogeochemistry and extraterrestrial biosignature detection.

High-altitude hydrothermal systems situated 4000 meters above sea level (a.s.l.), in mountainous regions on Earth constitute natural laboratories for studying fundamental biogeochemical processes. In the Andes, reduced atmospheric pressure could modulate gas-water exchange, which coupled to the physicochemical conditions produces comparable conditions to those proposed for early Earth environments[1–3]. Reconstruction of Archaean air pressure indicates values well below one atmosphere[3], reinforcing the relevance of such settings as analogues for early Earth conditions. These environments therefore offer direct insight into primitive redox-stratified cycles that may have shaped the emergence of metabolic pathways[4–6].

The Lirima hydrothermal system on the Chilean Altiplano Plateau (Fig. 1) exemplifies these conditions[7,8]. Operating at approximately 0.6 atm[9], this pressure is roughly half the present-day sea-level value and close to Archaean estimates of 0.4 to 0.5 atm[3]. At Lirima, gas-liquid partitioning influences the solubility of volatile compounds such as carbon dioxide and methane, thereby affecting their availability for microbial metabolism[8–10]. Although pressure has only a minor effect on equilibrium constants, it exerts a first-order control on the initial dissolved gas concentrations that fuel biogeochemical transformations[3]. At Lirima, the system features a temperature gradient from approximately 42 to 77 °C under reduced pressure conditions[7–9].

Microbial communities in hydrothermal systems demonstrably adjust their structure and metabolic strategies to local physicochemical gradients[8,11–13]. Chemical affinity, defined as the negative change in Gibbs free energy for a reaction at the activities prevailing in-situ, provides a quantitative measure of thermodynamic favorability along those gradients, and could serve as an approach to understand microbial-mediated metabolisms[11,14,15]. Previous work identified crossover points at which different redox reactions deliver identical energy as a function of pH[11]. However, it remains underexplored whether comparable temperature-driven crossover points occur under reduced atmospheric pressure, and whether any such convergence manifests as detectable shifts in microbial community structure and biogeochemical activity.

We address this knowledge gap by combining characterization of water physiochemistry and geochemistry (Fig. 2a, b), thermodynamic equilibrium modelling (Fig. 2c) validated with independent geochemical data[7] (Fig. 2d), stable isotope measurements (Fig. 2e) elemental composition of sedimentary organic matter (Fig. 2f), in-situ ^{3}H-leucine incorporation rates (Fig. 2f), and dereplicated high-quality metagenome-assembled genomes (MAGs;

A full list of affiliations appears at the end of the paper. e-mail: mhengst@ucn.cl

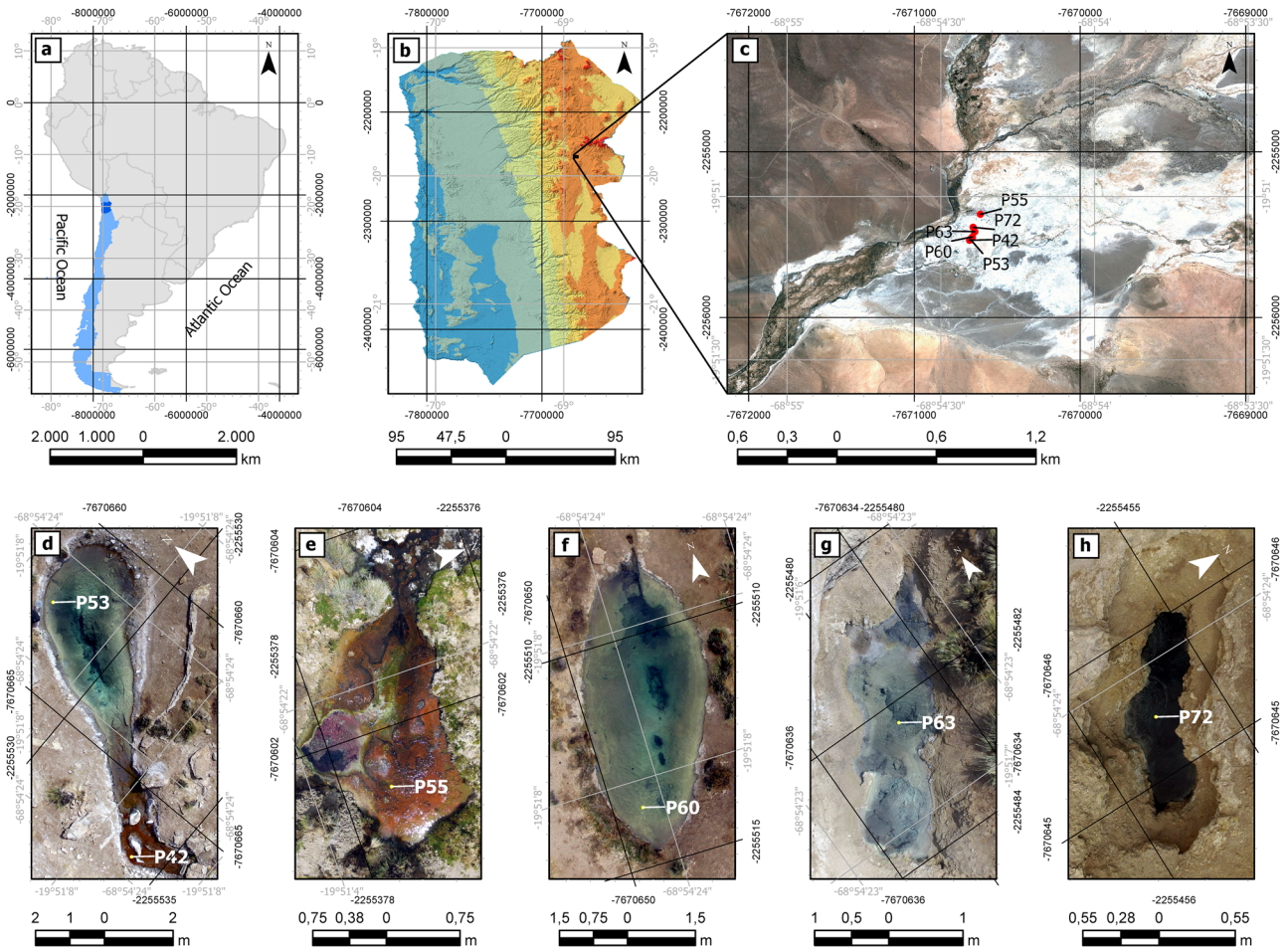

Fig. 1 | Geographical context and hydrothermal pool characterization. a Location map showing Chile (blue) and the Tarapacá region (dark blue) in South America. **b** Digital elevation model of the Tarapacá region highlighting the high-altitude study area. **c** Satellite image of the Lirima hydrothermal system showing the distribution of studied pools (P42-P72). **d**–**h** High-resolution drone imagery of individual pools arranged along the thermal gradient (53–75 °C). **d** P42 and P53 pools showing clear redox zonation. **e** P55 pool displaying distinctive microbial mat coloration; (**f**), P60 pool; (**g**), P63 pool; and (**h**), P72 pool exhibiting the highest temperature. White arrows indicate north orientation. Scale bars indicate distance in kilometers (**a**–**c**) and meters (**d**–**h**) (See Supplementary Note 1 for detailed map and image creation information).

Fig. 2f) along the temperature gradient found within the Lirima system. We identify an energetic convergence node (ECN) between 63 and 64 °C, where chemical affinities of hydrogenotrophic and carboxydotrophic methanogenesis converge with sulfate reduction. Isotopic shifts in $\delta^{13}C_{(VPDB)}$ and $\delta^{34}S_{(VCDT)}$ across this interval corroborate the predicted transition in dominant metabolic processes[12,13,16–18], whilst concurrent changes in protein synthesis rates, elemental compositions, functional gene and metabolic modules presence demonstrate that theoretical energetic convergence could translate directly into fundamental reorganization of microbial community structure and metabolism.

By extending the thermodynamic crossover point concept to temperature in a low-pressure hydrothermal setting, our study illuminates how energy landscapes influence metabolic distribution and evolution. The ECN framework also informs the search for biosignatures in extraterrestrial hydrothermal environments such as those postulated for Enceladus and Europa, where comparable energy-driven transitions may occur[19,20]. Finally, it provides a theoretical basis for assessing chemical and biological complexity in off-Earth analogue systems[21], offering additional constraints on biogeochemical cycling under conditions akin to those on early Earth.

Results and discussion

Biogeochemical fingerprint characterization

The Lirima hydrothermal field (4000 m a.s.l.; Tarapacá Region, Chile; Fig. 1) exhibits a well-defined redox gradient that spans suboxic surface waters and anoxic sediments[7,8,22]. Pool temperatures range from 53 to 75 °C, while pH remains circum-neutral (6.2–7.3). Electrical conductivity varies between 1.73 and 2.13 mS cm^{-1} and in-situ oxidation-reduction potential (ORP) is consistently below −150 mV (Table 1; Supplementary Table 1). Temperature correlates significantly with pH ($\tau = -0.59$, $p < 0.01$; Supplementary Table 2) and with oxidation-reduction potential ($\tau = -0.73$, $p < 0.01$; Supplementary Table 2), delineating a continuous gradient comparable to those proposed for Archaean systems where carbon–sulfur biogeochemical networks may have developed[1,3,4,6].

At reduced atmospheric pressure (~0.6 atm[9]), the system displays specific gas–water–sediment interactions characteristic of high-altitude hydrothermal environments. Dissolved CO_2 concentration exceeds CH_4 by two orders of magnitude (Table 1; Supplementary Table 1), and these gases demonstrate significant correlation ($\tau = 0.90$, $p < 0.01$; Supplementary Table 2), which may indicate linked hydrogenotrophic methanogenesis and anaerobic methanotrophy[23,24]. PHREEQC simulations, constrained by measured temperature, pH, ORP, and geochemical composition including dissolved CO_2 and CH_4, indicate that the waters are undersaturated in CO_2(g), CH_4(g) and other gases (Supplementary Table 3).

Chemical activities of H_2(aq) and H_2S(aq) were derived from speciation modelling, as direct field measurements were not feasible. This approach aligns with previous studies that quantify, compare and analyze speciation models using PHREEQC[25], and *llnl.dat* thermodynamic database under similar conditions to those presented in this study[26,27]. The standard

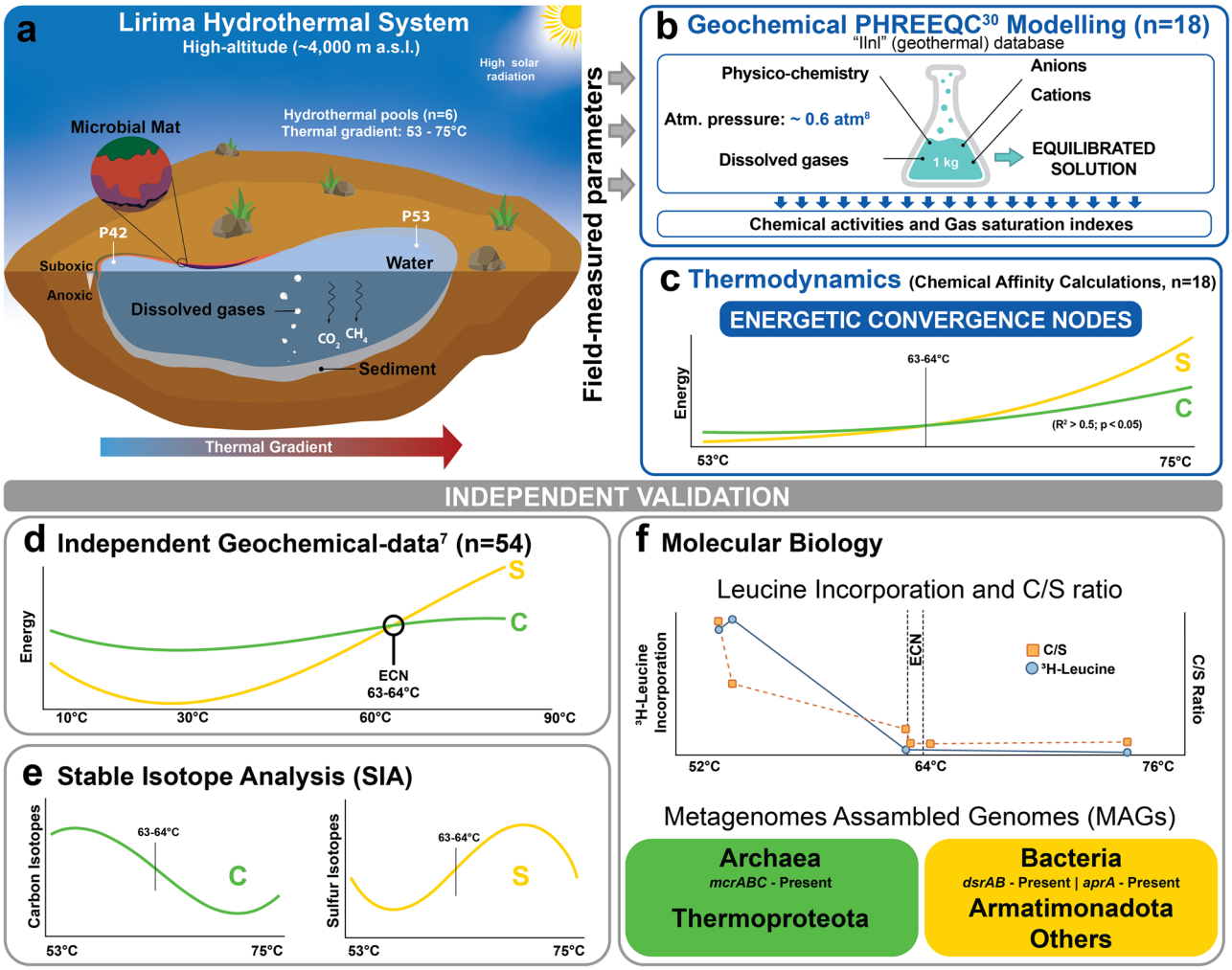

Fig. 2 | Conceptual illustration of hydrothermal system characterization and ECN analysis. a High-altitude hydrothermal pools (> 4000 m a.s.l.) showing thermal gradients and biogeochemical zonation. **b** Field parameters used in geochemical modelling (PHREEQC) for chemical affinity calculations ($n = 18$). **c** Temperature-dependent energy distributions and primary ECN between methanogenesis and sulfate reduction reactions. **d** Independent thermodynamic validation with previously obtained dataset[7] ($n = 54$). **e** Stable isotope analyses of sediment organic matter ($n = 18$). **f** Integration of in-situ ^{3}H-leucine incorporation experiments, sediment organic matter C/S ratios, and metagenomic validation of potential metabolic pathways through high-quality metagenome-assembled genomes.

practices and methodological considerations for geothermal fluids are detailed in Methods. The observed undersaturation suggests these gases function as volcanic and biogenic sinks along suboxic gradients[28,29].

The *llnl.dat* thermodynamic database in PHREEQC derives from the Lawrence Livermore National Laboratory EQ3/6 compilation and implements revised Helgeson-Kirkham-Flowers equations of state, enabling confident extrapolation of equilibrium constants to 300 °C[30]. Benchmark evaluations against experimental data from deep geothermal brines demonstrate that *llnl.dat* reproduces mineral saturation indices to within ±0.2 log units across temperatures of 25 to 250 °C, outperforming other databases in chloride-rich hydrothermal fluids[26,31]. Independent reactive transport simulations of hydrogen storage caverns and fractured geothermal reservoirs confirm consistent agreement between calculated aqueous activities and field observations, establishing *llnl.dat* as the preferred computational framework for high-temperature geochemical applications[25,27,32].

The aqueous chemistry is dominated by SO_4^{2-} relative to Cl^- and HCO_3^-, positioning the fluids between immature sulfate-rich and mature chloride-rich waters observed in ternary diagrams (Supplementary Fig. 1a). The high SO_4^{2-} concentration supports dissolution of H_2S(aq) (Supplementary Fig. 1a, Supplementary Fig. 1b). Bicarbonate (HCO_3^-) shows a significant negative correlation with dissolved CO_2 and CH_4 (Supplementary Table 2), whereas major cation concentrations followed the trend $Na^+ > Ca^{2+} > K^+ > Li^+ > Mg^{2+}$ (Supplementary Table 1), reflecting substantial hydrothermal input moderated by late-stage gas–water–rock reactions[7].

Trace-element distributions further illustrate the physicochemical zonation. In the aqueous phase, As and Mn were the dominant elements, while other metals (Fe, Cu, Zn, and Pb) and Sb showed concentrations below the detection limit (0.4 µg L^{-1}; Table 1; Supplementary Table 1). However, sediments contained significant amounts of Fe (up to 5.2 g kg^{-1}), followed by As (Table 2; Supplementary Table 1) and Sb, both of which were highly enriched when compared to the current concentration of As (5.7 mg/kg) and Sb (0.75 mg/kg) in the Upper Continental Crust (UCC)[33]. Significant positive correlations between sedimentary Fe and other redox elements (As, Mn; $\tau = 0.60–0.63$, $p < 0.01$; Supplementary Table 2) indicate conditions that may support couple redox cycling. The prevalence of Fe could act as an electron acceptor facilitating anaerobic methane oxidation[34]. This process has been documented in similar hydrothermal[35,36] and wetland[37] environments, where iron minerals enable methanotrophic archaea to oxidize methane[34]. Similarly, ammonium could be oxidized by Fe through Feammox process, which was identified in natural and anthropogenic systems, related with a consortium of microorganisms, linking Fe/N and Fe/C cycles[38,39]. Elevated temperatures enhance mineral dissolution and thus promote mobilization of As and Fe from both hydrothermal fluids and sediments[34,40–42].

Table 1 | Physical and biogeochemical characterization of waters from Lirima hydrothermal system

Analyte	Unit	P42	P53	P55	P60	P63	P72
T	°C	53.4 ± 0.6	62.9 ± 1.2	54.3 ± 1.1	63.2 ± 0.4	64.5 ± 0.2	74.6 ± 0.2
pH	-	7.2 ± 0.2	6.6 ± 0.1	6.5 ± 0.1	6.6 ± 0.1	6.4 ± 0.1	6.3 ± 0.2
EC	mS cm^{-2}	1943.3 ± 185.0	1753.3 ± 5.8	1903.3 ± 170.1	1833.3 ± 85.0	1836.7 ± 92.9	1760 ± 43.6
ORP	mV	−181.7 ± 7.6	−273.3 ± 20.8	−256.7 ± 5.8	−270 ± 10	−270 ± 10	−326.7 ± 5.8
HCO_3^-	mg L^{-1}	235 ± 49.2	171.7 ± 45.4	113.3 ± 5.8	193.3 ± 20.8	170.0 ± 30.0	156.7 ± 11.5
Cl^-	mg L^{-1}	273.3 ± 32.1	266.7 ± 49.3	303.3 ± 70.2	303.3 ± 11.5	236.7 ± 25.2	278.3 ± 10.4
SO_4^{2-}	mg L^{-1}	553.3 ± 115.0	550 ± 85.4	796.7 ± 75.1	926.7 ± 60.3	390.0 ± 10.0	426.7 ± 20.8
Na^+	mg L^{-1}	463.3 ± 65.1	418.3 ± 50.1	588.3 ± 92.5	640 ± 43.6	313.3 ± 25.2	326.7 ± 37.9
K^+	mg L^{-1}	37.7 ± 2.5	38.7 ± 5	32 ± 0	39.7 ± 2.1	38.3 ± 0.6	33 ± 2
Ca^{2+}	mg L^{-1}	51.7 ± 7.6	53.7 ± 4.2	44 ± 5	58 ± 3.6	54.3 ± 6.4	48.7 ± 5.8
Mg^{2+}	mg L^{-1}	2.8 ± 0.8	3 ± 0.5	2 ± 0	2.7 ± 0.8	2.3 ± 0.3	2.3 ± 0.6
Li^+	mg L^{-1}	3.8 ± 0.3	4.7 ± 0.6	4 ± 0.5	4.5 ± 0.5	4.6 ± 0.5	3.3 ± 0.5
As	µg L^{-1}	116.7 ± 20.8	136.7 ± 25.2	56.7 ± 11.5	33.3 ± 5.8	136.7 ± 15.3	13.3 ± 5.8
Cu	µg L^{-1}	ND	ND	ND	ND	ND	ND
Fe	µg L^{-1}	ND	ND	ND	ND	ND	ND
Mn	µg L^{-1}	93.3 ± 20.8	90 ± 17.3	83.3 ± 11.5	100 ± 20	106.7 ± 5.8	83.3 ± 11.5
Pb	µg L^{-1}	ND	ND	ND	ND	ND	ND
Sb	µg L^{-1}	ND	ND	ND	ND	ND	ND
Zn	µg L^{-1}	ND	ND	ND	ND	ND	ND
CO_2	µM	515.5 ± 34.6	538.7 ± 55.1	1591.2 ± 17.1	793.1 ± 34.4	1054.3 ± 404.3	1438.1 ± 62.8
CH_4	µM	4.6 ± 0.4	6.8 ± 0.7	27.2 ± 3.6	11.1 ± 0.5	15.7 ± 5.9	19.2 ± 1.1

Water physico-chemistry, major ions, trace elements and dissolved gases. Values represent mean ± standard deviation from triplicate analyses.
ND indicates concentrations below detection limits (<0.4 µg L^{-1} in water samples).

Table 2 | Sediment characterization of the Lirima hydrothermal system

Analyte	Unit	P42	P53	P55	P60	P63	P72
As	mg kg^{-1}	20 ± 1.7	406.1 ± 81.3	129.8 ± 29.6	30.4 ± 6.3	99 ± 3.3	99.8 ± 2.2
Cu	mg kg^{-1}	5.6 ± 0.3	14 ± 4.1	12.0 ± 3.0	14.5 ± 3.0	10.3 ± 1.3	4.8 ± 0.4
Fe	gr kg^{-1}	1.8 ± 0.3	5.2 ± 1.3	3.0 ± 0.2	0.6 ± 0.0	1.4 ± 0.1	2.2 ± 0.2
Mn	mg kg^{-1}	55.6 ± 7.9	67.9 ± 17	48.4 ± 13.6	11.2 ± 0.5	29.2 ± 3.3	38.7 ± 1.4
Pb	mg kg^{-1}	3.2 ± 0.8	3.2 ± 0.9	3.6 ± 0.8	2.8 ± 0.3	2.8 ± 0.8	2.4 ± 0.4
Sb	mg kg^{-1}	ND	53.7 ± 2.4	ND	7.6 ± 0.8	10.3 ± 0.3	38.1 ± 0.7
Zn	mg kg^{-1}	13.4 ± 1.9	21.3 ± 4.9	26.1 ± 7.5	5.9 ± 0.5	10.5 ± 0.3	7.8 ± 0.1
$\delta^{13}C_{(VPDB)}$ Corrected	‰	−17.24 ± 0.61	−20.89 ± 0.54	−18.02 ± 1.18	−22.33 ± 0.33	−27.19 ± 0.71	−26.53 ± 1.44
$\delta^{34}S_{(VCDT)}$	‰	−11.87 ± 2.08	−12.73 ± 0.22	−19.81 ± 0.71	−11.28 ± 0.45	−10.83 ± 0.14	−10.25 ± 1.09
%C	%	5.21 ± 1.17	2.92 ± 0.28	4.36 ± 0.70	0.81 ± 0.17	0.45 ± 0.05	0.64 ± 0.25
%S	%	0.63 ± 0.05	1.88 ± 0.04	0.99 ± 0.05	1.29 ± 0.36	0.73 ± 0.04	0.87 ± 0.03
C/S	-	8.31 ± 2.04	1.56 ± 0.14	4.41 ± 0.88	0.67 ± 0.27	0.62 ± 0.10	0.74 ± 0.31

Trace element concentrations and organic matter characterization through carbon ($\delta^{13}C_{(VPDB)\ Corrected}$) and sulfur ($\delta^{34}S_{(VCDT)}$) isotopes, with elemental composition (%C, %S) and C/S ratios. Values represent mean ± standard deviation from triplicate analyses.
ND indicates concentrations below detection limits (<0.3 mg kg^{-1} in sediment samples).

Temperature appears to be the principal driver of biogeochemical change, a pattern most clearly reflected in the stable isotopes of organic matter (Table 2, Supplementary Table 1). Sedimentary $\delta^{13}C_{(VPDB)}$ values decrease from −17.2‰ to −27.7‰ with rising temperature, whereas $\delta^{34}S_{(VCDT)}$ values shift from strongly depleted (−20.5‰) to less negative (−9.1‰) at ~63–64 °C. Concurrently, carbon-to-sulfur ratios fall from 8.31 ± 2.0 to <1.0 (Table 2, Supplementary Table 1) across the same interval, indicating enhanced sulfur incorporation into sediments. Together, these geochemical and isotopic trends suggest a temperature-controlled transition in dominant metabolic processes[43–45].

Anoxic thermodynamic convergence

Our analysis reveals distinct thermal zones in hydrothermal pools where multiple metabolic pathways achieve similar chemical affinities (Fig. 3a), which we termed Energetic Convergence Nodes (ECNs). These ECNs arise from intersections among carbon and sulfur reaction pathways detailed in

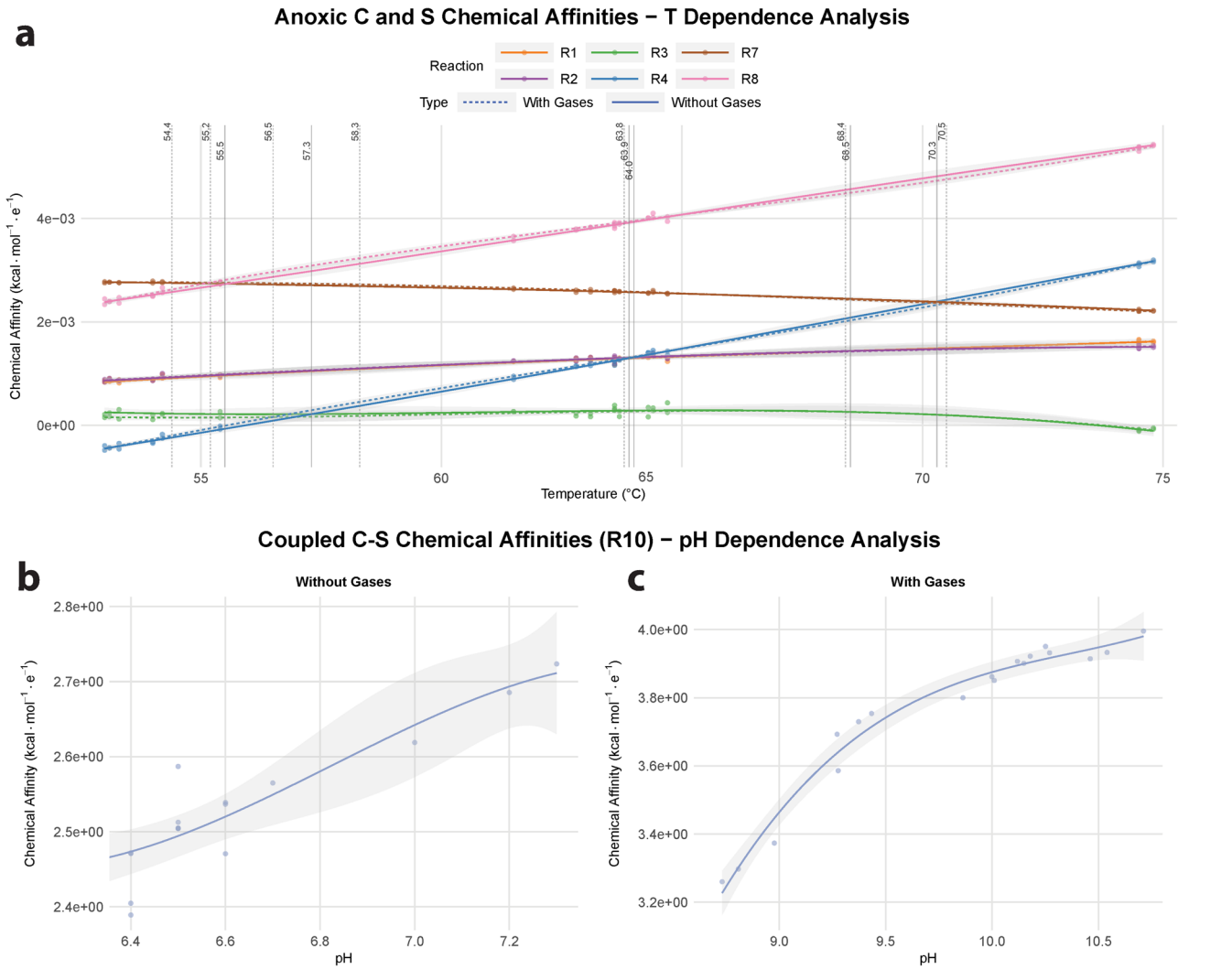

Fig. 3 | Thermodynamic analysis of chemical affinities across the thermal gradient. a Temperature dependence of chemical affinities for individual methanogenic (R1, R2, R3) and sulfur-reducing (R4, R7, R8) reactions, showing Energetic Convergence Nodes (ECN) at specific temperatures (vertical lines). Solid and dashed lines represent simulations without and with dissolved gases, respectively. **b**, **c** pH dependence of coupled carbon-sulfur reaction (R10: $CH_4 + SO_4^{2-} \rightarrow CO_2 + H_2S + 2H_2O$) showing two distinct equilibrium regimes: circumneutral pH without dissolved gases (**b**) and alkaline pH with dissolved gases (**c**). All trends were fitted using cubic functions and Kendall correlated ($p \leq 0.05$).

Table 3, highlighting temperature-dependent interactions of potential abiotic and biotic processes under the conditions observed in high-altitude hydrothermal environments.

For clarity, only CO_2 and CH_4 were directly measured in this study; activities for H_2, CO and reduced sulfur species were estimated via PHREEQC speciation using the "*llnl.dat*" geothermal database (Supplementary Table 4) under our measured initial conditions (Table 1, Supplementary Table 1).

This approach provides a theoretical framework for calculating the energy present in the system based on solution geochemistry, both with and without inclusion of CO_2 and CH_4 gases to verify the accuracy of chemical affinities.

Similar computational approaches have been successfully employed in diverse hydrothermal systems, including Yellowstone[46], Icelandic geothermal fields[47], and volcanic crater lakes[7]. The validity of this computational approach for the Lirima system is demonstrated by the consistency between scenarios incorporating measured gaseous species (CO_2, CH_4) and those relying solely on speciation calculations, indicating accurate representation of the thermodynamic state studied in this research[48].

Comparative thermodynamic modelling including (wG) and not including (woG) the measured CO_2 and CH_4 gases used as input, reveals significant variations in pH, reduction potential (pe) and individual species activities (Supplementary Tables 4, 5), highlighting the importance of gas measurements for accurate speciation[49]. To test the robustness of our chemical affinity calculations under both scenarios, we confirmed that the relative ordering of the resulting chemical affinities remains stable (Supplementary Tables 6–8).

Statistical assessments using Kendall's τ (Supplementary Table 9) and cubic regressions (Supplementary Table 10) confirm significant, non-linear relationships between temperature and affinity for thermally dominated reactions ($p \leq 0.01$; cubic $R^2 > 0.8$, $p \leq 0.01$). In contrast, coupled sulfate-dependent methane oxidation (R10) exhibits a stronger pH dependence ($\tau > 0.74$, $p < 0.01$; Fig. 3b, c).

These cubic fits arise from the intrinsic temperature dependence of standard Gibbs free energies employed in chemical affinity calculations[15].

Comparison of chemical affinities calculated from water-only geochemistry (woG) against those including the measured gases (wG) revealed no significant differences in chemical affinity values (ANOVA One-Way

Table 3 | Carbon and sulfur reaction pathways under anoxic conditions

R	Chemical equation	e-	Abiotic name	Biotic name
1	$CO_{2(aq)} + 4H_{2(aq)} <-> CH_{4(aq)} + 2H_2O_{(l)}$	8	Sabatier reaction (carbon dioxide hydrogenation to methane)	Hydrogenotrophic methanogenesis (by archaea)
2	$CO_{(aq)} + 3H_{2(aq)} <-> CH_{4(aq)} + H_2O_{(l)}$	6	Methanation of carbon monoxide (carbon monoxide hydrogenation to methane)	Carbon monoxide methanogenesis
3	$4CO_{(aq)} + 2H_2O_{(l)} <-> CH_{4(aq)} + 3CO_{2(aq)}$	6	Shift reaction (or Water-gas shift methanation)	Carboxydotrophic methanogenesis
4	$SO_4^{2-} + 4H_{2(aq)} + 2H^+ <-> H_2S_{(aq)} + 4H_2O_{(l)}$	8	Reduction of sulfate to hydrogen sulfide	Sulfate reduction (by sulfate-reducing bacteria)
5	$4SO_3^{2-} + 2H^+ <-> 3SO_4^{2-} + H_2S_{(aq)}$	6	Disproportionation of sulfite	Sulfite reduction (reducers)
6	$SO_3^{2-} + 3H_{2(aq)} + 2H^+ <-> H_2S_{(aq)} + 3H_2O_{(l)}$	6	Reduction of sulfite to hydrogen sulfide	Sulfite reduction (by sulfite-reducing bacteria)
7	$S_2O_3^{2-} + H_2O_{(l)} <-> SO_4^{2-} + H_2S_{(aq)}$	8	Hydrolysis of thiosulfate	Thiosulfate reduction (by sulfur-reducing bacteria)
8	$S_2O_3^{2-} + 2H^+ + 4H_{2(aq)} <-> 2H_2S_{(aq)} + 3H_2O_{(l)}$	8	Reduction of thiosulfate with hydrogen	Thiosulfate reduction with hydrogen
9	$4S_2O_4^{2-} + 4H_2O_{(l)} <-> 3H_2S_{(aq)} + 5SO_4^{2-} + 2H^+$	15	Decomposition of dithionite	Dithionite reduction (by sulfur bacteria)
10	$CH_{4(aq)} + SO_4^{2-} <-> CO_{2(aq)} + H_2S_{(aq)} + 2H_2O_{(l)}$	8	Sulfate-dependent methane oxidation	ANME-SRB mediated methane oxidation

Reactions include both abiotic and biotic routes for carbon reduction (R1-R3), sulfur reduction (R4-R9), and coupled S-C processes (R10). Electron transfer numbers (e^-) represent the number of electrons involved in each reaction[15].

Activities of species like H_2, CO, and H_2S were derived from PHREEQC speciation calculations constrained by measured system parameters (temperature, pH, ORP and aqueous geochemistry) using the *llnl.dat* thermodynamic database. This approach is established in geochemical studies of geothermal systems[113] and validated through field studies showing predicted activities typically aligned with measured concentrations within ±0.2–0.5 log units[48]. Thermodynamic modelling provides a consistent framework for evaluating energetic landscapes[11,114]. The consistency between calculated ECN temperatures across scenarios (with and without measured CO_2 and CH_4 gases, ΔECN < 1 °C) provides additional validation of this approach for identifying metabolically relevant transitions.

test $p > 0.05$; Supplementary Table 8). Moreover, all ECN temperatures shifted by less than 1 °C between scenarios (Supplementary Table 11), confirming that PHREEQC-based affinity calculations reliably approximate available energy regardless of direct gas measurements when using geochemical water composition and physiochemistry parameters.

Chemical affinity trends along the 53–75 °C gradient (Fig. 3a) reveal distinct temperature dependencies. Hydrogenotrophic methanogenesis (R1 and R2) and several sulfate-reduction pathways (R4, R6, R8) become increasingly favorable with temperature, whereas reductions of sulfite (R5), thiosulfate (R7) and dithionite (R9) grow progressively unfavorable (Fig. 3a; Supplementary Tables 6–7). Carboxydotrophic methanogenesis (R3) maintains relatively constant affinity, while R10 is modulated by pH (Fig. 3b, c), consistent with previous findings[11].

Our chemical affinity calculations identify specific ECNs at: 55–56 °C (R7/R8), 56–57 °C (R3/R4), 63–64 °C (R1–R2/R4; principal ECN), 68–69 °C (R1/R2) and 70–71 °C (R4/R7) (Fig. 3a; Supplementary Table 11). These nodes delineate temperature windows in which competing pathways yield identical affinities, suggesting points of potential metabolic transition.

Calculated energy densities (Supplementary Tables 12–13) are sensitive to the limiting reactant (Supplementary Table 14), particularly measured dissolved CO_2 and CH_4 gases, yet carbon- and sulfate-reducing reactions (R1, R2, R4) maintain positive densities across all conditions (Supplementary Tables 15–16). The coupled anaerobic methane oxidation and sulfate reduction pathway (R10) displays a more complex setting, reflecting thermodynamic trade-offs between yield and substrate limitation. This analysis demonstrates potential interactions among individual and coupled metabolic pathways, suggesting adaptive strategies aligned with environmental energetic constraints. The interplay is particularly evident in anaerobic oxidation of methane (AOM) coupled to sulfate reduction (SR), which responds to environmental pH shifts[50].

To test the broader applicability of our energetic convergence framework, we applied the same thermodynamic approach to an independent high-altitude dataset ($n = 54$) from geothermal systems operating under comparable conditions (>4000 m a.s.l.; <0.6 atm)[7]. This validation dataset encompasses geochemistry from Surire, Puchuldiza–Tuja, Pampa Lirima, Pampa Apacheta, El Tatio and Torta de Tocorpuri (Supplementary Table 17)[7], spanning a wider thermal gradient (7.4 to 87.6 °C) than our primary Lirima dataset ($n = 18$).

Using the same PHREEQC v3 procedure[30], we calculated chemical affinities for reactions R1-4 and R7-8 (Supplementary Table 18; Table 3, Fig. 3a). This analysis confirms that the energetic convergence concept is not site-specific to the Lirima system.

Across this extended dataset ($n = 54$) the affinities of R1, R2 and R4 intersect reproducibly between 63 and 64 °C, identical to the primary ECN (Supplementary Fig. 2). The cubic slope of the affinity curves surrounding the node is likewise comparable (Supplementary Table 19), indicating that crossover results principally from intrinsic thermodynamic properties of the reactions rather than local fluid composition. This pattern persists despite substantial variation in physicochemical and geochemical parameters (Supplementary Table 17), suggesting that temperature-controlled convergence exerts a first-order control on electron-donor partitioning in anoxic fluids.

Ten samples from this subset yielded incomplete results (Supplementary Table 18). Six displayed considerable nitrate concentrations that, coupled with the prevailing physiochemistry (temperature and pH) could influence oxidizing conditions, where nitrate becomes the preferred electron acceptor and suppresses both methanogenesis and sulfate reduction[51,52]. In the remaining four samples pH was below 4 and reported bicarbonate was below quantification limits[7]. At these acidities, inorganic carbon exists almost exclusively as dissolved CO_2, precluding reliable calculation of CO_2-reducing reactions[53,54]. The inability to calculate complete chemical affinities for these samples underscores that redox speciation and carbonate chemistry are fundamental determinants of system energetics, controlling whether solutions favor oxidative or reductive routes.

Notwithstanding these specific geochemical constraints, the recurrence of an identical convergence temperature window (Supplementary Fig. 2) across six geologically and hydrologically distinct geothermal contexts provides strong external validation of the ECN framework (Fig. 3). This result implies that the 63–64 °C threshold identified at Lirima represents a broader ecological boundary for anaerobic carbon- and sulfur-based metabolisms in reduced, high-altitude hydrothermal waters.

These ECNs establish a quantitative framework for interpreting redox transitions in high-altitude hydrothermal systems, emphasizing temperature and pH as critical factors shaping metabolic regimes. The biological significance of these thermodynamic predictions is validated through isotopic and community analyses presented in the following section.

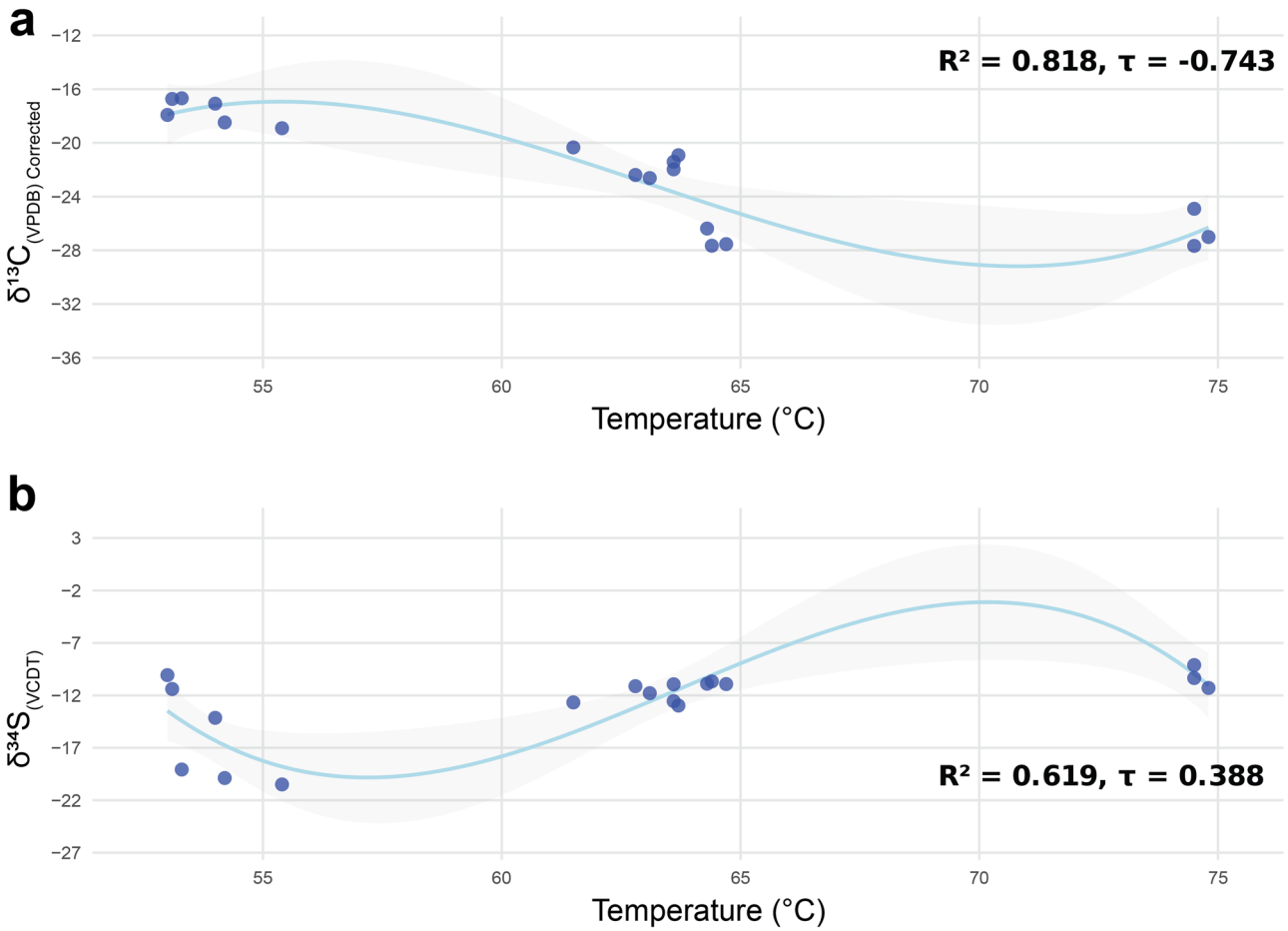

Fig. 4 | Temperature-dependent metabolic transitions revealed through isotopic signatures. a Carbon isotopes ($\delta^{13}C_{(VPDB)\ Corrected}$) showing progressive depletion with temperature. **b** Sulfur isotopes ($\delta^{34}S_{(VCDT)}$) displaying transition from more depleted to less depleted values at 63–64 °C. Blue dots represent measurements; light blue lines show statistically significant cubic regressions ($p \leq 0.05$).

Isotopic evidence from organic matter

Stable-carbon and sulfur isotope analyses of sedimentary organic matter independently corroborate the Energetic Convergence Nodes (ECN) derived from chemical affinity calculations, revealing temperature-dependent shifts in microbial metabolic regimes within the high-altitude hydrothermal gradient.

Temperature exerts strong influence on carbon isotopic composition (Fig. 4). Following the cubic temperature-affinity relationships observed in thermodynamic calculations, we applied equivalent cubic regression models to isotopic data to assess parallel non-linear behavior, validated with non-parametric Kendall's τ analyses (Supplementary Table 20).

Corrected $\delta^{13}C_{(VPDB)}$ (Fig. 4a) shows significant negative correlation with temperature ($\tau = -0.743$, $p < 0.01$, Supplementary Table 20) with cubic fit explaining 81.8% of variance ($R^2 = 0.818$, $p < 0.01$, Supplementary Table 20). Sedimentary $\delta^{34}S_{(VCDT)}$ (Fig. 4b) demonstrates moderate positive correlation ($\tau = 0.388$, $p < 0.05$, Supplementary Table 20) with temperature, with cubic model accounting for 61.9% of variability ($R^2 = 0.619$, $p = 3.01 \times 10^{-3}$, Supplementary Table 20). Carbon-to-sulfur ratios (C/S) correlate negatively ($\tau = -0.651$, $p < 0.01$, Supplementary Table 20) and follow cubic trends, capturing 90.9% of variance ($R^2 = 0.909$, $p = 1.52 \times 10^{-7}$, Supplementary Table 20). These statistics confirm both the strength and the non-linear nature of isotopic and elemental transitions across the thermal gradient.

Corrected $\delta^{13}C_{(VPDB)}$ values decrease from −17.9‰ at ~53 °C to −27.7‰ at ~64 °C (Fig. 4a), coinciding with the principal ECN at 63–64 °C (Fig. 3a), between hydrogenotrophic methanogenesis and sulfate reduction (R1, R2 and R4, Table 3). This 10‰ depletion may indicate a shift from autotrophic carbon fixation towards pathways yielding more isotopically light biomass or by-products[55,56]. Despite continued thermodynamic favorability of carbon-reducing reactions at these temperatures, total organic carbon content falls below 1% in the hottest pools (Table 2; Supplementary Table 1), consistent with diminished net autotrophy under extreme conditions.

Sedimentary $\delta^{34}S_{(VCDT)}$ values rise from ~−20.5‰ in cooler pools to ~−10.8‰ at the ECN (Fig. 4b), reflecting ~9.7‰ enrichment that mirrors the cubic-regression trend (Supplementary Table 20). This enrichment could indicate increased sulfate respiration at higher temperatures[43,57], corroborated by sedimentary sulfur content increasing from ~2% to 4–6% (Table 2; Supplementary Table 1).

C/S ratios decrease from ~10.0 to <1.0 at 63–64 °C (Table 2; Supplementary Table 1), marking a shift from carbon-dominated to sulfur-dominated processes. In intermediate pools (55–62 °C), C/S values of 0.5–1.7 indicate concurrent carbon- and sulfur-based metabolisms[58,59].

These isotopic and elemental proxies, supported by significant statistical relationships, demonstrate the connection between temperature-dependent thermodynamic constraints and microbial metabolic responses. The alignment of these proxies with ECN provides insight into how microbes balance energy yield and metabolic flexibility in extreme, pressure-constrained environments, with implications for early-Earth analogue systems[60,61].

The observed decrease in C/S ratios above 63–64 °C likely reflects multiple factors beyond thermodynamic constraints. Temperature

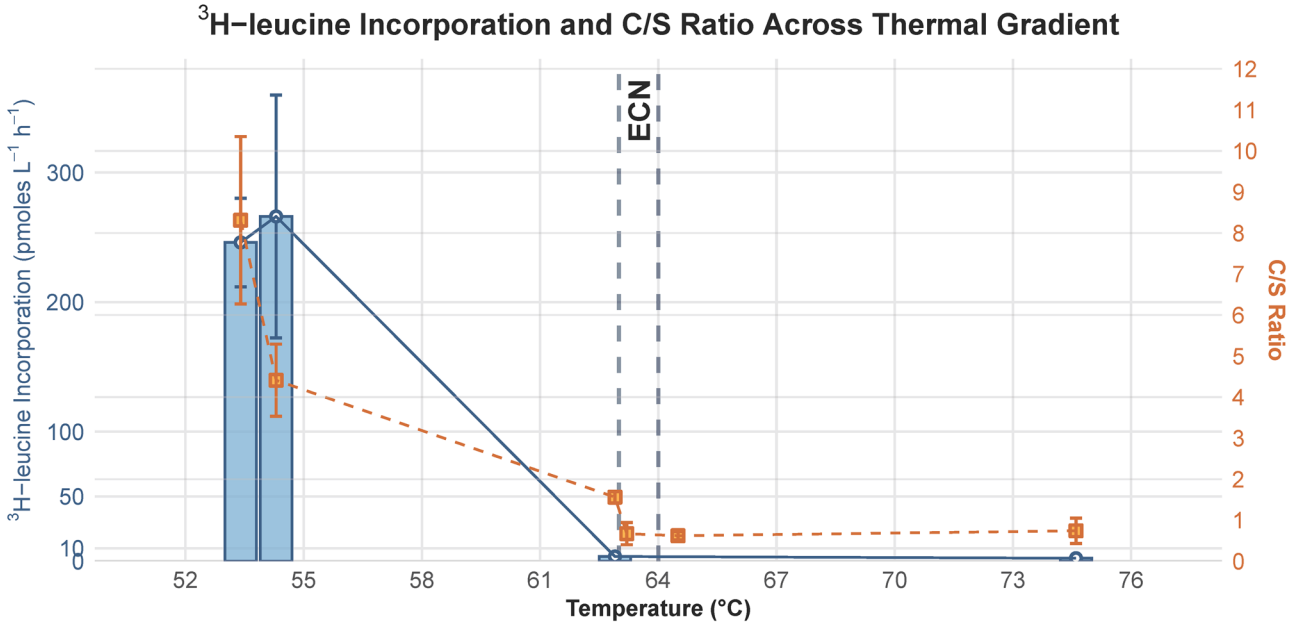

Fig. 5 | Metabolic activity and sediment organic-matter elemental composition transitions across the thermal gradient. ^{3}H-leucine incorporation rates (blue bars) and carbon-to-sulfur ratios (orange dashed line) measured across hydrothermal pools P42 to P72. All measurements performed in triplicate ($n = 3$).

represents an established physiological barrier for photosynthetic microorganisms, with most cyanobacterial and algal taxa showing upper thermal limits between 60 and 65 °C[62,63]. This thermal threshold correlates with our observed ECN and the absence of visible microbial mats in the hottest pools (Fig. 1g, h).

The shift from carbon-dominated to sulfur-dominated metabolism thus represents both a thermodynamic response and community composition change, where phototrophs may be replaced by chemolithoautotrophs. These chemolithoautotrophs likely employ diverse metabolic pathways to thrive in temperature-dependent energetic landscapes, prioritizing thermodynamically favorable pathways as conditions change[64,65]. The concordance between thermodynamic calculations and isotopic transitions suggests that even in the absence of photoautotrophs, specialized thermophiles adjust their carbon and sulfur metabolism in response to energetic constraints.

We acknowledge that thermodynamic constraints alone do not fully account for organic matter signatures observed above the ECN. Previous work demonstrated the presence of active phototrophs in this hydrothermal system, with community structure mainly shaped by geochemical and physicochemical gradients[8]. To address this complexity, we conducted integrative studies combining genomic analyses using metagenome-assembled genomes (MAGs) to resolve potential carbon and sulfur metabolic capacities alongside energetic feasibility, and microbial activity experiments through in-situ ^{3}H-leucine incorporation with full solar radiation. These combined approaches help differentiate between community composition effects and thermodynamic drivers of metabolic transitions.

Preliminary biological activity and molecular evidence

Planktonic microbial incubations conducted in-situ using ^{3}H-leucine across the temperature gradient found in Lirima demonstrate a pronounced temperature dependence of heterotrophic protein synthesis (Fig. 5). Incorporation rates remain high between 52 and 55 °C, ranging from 250 to slightly above 300 pmol L^{-1} h^{-1}. At 64 °C, rates collapse to ≤3 pmol L^{-1} h^{-1} and remain negligible up to 75 °C (Supplementary Table 21).

Leucine uptake is a recognized proxy for bacterial protein synthesis and production in natural waters[66], and its abrupt decline beyond physiological optima has been observed for marine bacterioplankton[67] and for microbial assemblages inhabiting hydrothermal plumes[68]. The coincidence between this functional collapse and the temperature at which thermodynamic modelling predicts equality in affinities of methanogenesis and sulfate reduction supports the interpretation that ECN provides an alternative perspective on physiological boundaries.

The elemental record measured in sediment organic matter conveys an analogous signal. Carbon-to-sulfur ratios (C/S) sediments (Fig. 5) remain between 8 and 10 below 60 °C (Table 2, Supplementary Table 1), indicating carbon-centered diagenesis, but fall to values below 1 at and above 64 °C. Such low ratios typify environments dominated by sulfate reduction and pyrite formation[69,70]. The elemental transition therefore archives the long-term geochemical memory of the same metabolic shift that the ^{3}H-leucine assay captures in real time (Supplementary Table 21).

Thermodynamic modelling predicts that hydrogenotrophic methanogenesis (reactions R1–R2 in Fig. 3a) is favorable up to the ECN at 63–64 °C, whereas canonical dissimilatory sulfate reduction (R4) becomes energetically preferred above this threshold (Table 3; Supplementary Table 7). To assess the presence of metabolic pathways predicted to be thermodynamically favorable, we reconstructed community genomes (MAGs) from Lirima pools.

Metagenomic co-assembly of triplicate sediment and microbial mat samples from pools P42, P53 and P60 yielded 340 high-quality (HQ) metagenome-assembled genomes. Dereplication of the 340 total high-quality assemblies yielded 182 non-redundant bins across triplicate samples from each pool and matrix type, of which 103 harbored complete or near-complete marker gene sets for methanogenesis, sulfate reduction, or sulfite reduction (Table 4).

Methanogenic potential occurs exclusively in dereplicated MAGs recovered close to ECN. These bins possess the methyl-coenzyme M reductase complex (*mcrABC*), a reliable functional marker for methane production in environmental samples[71–73]. Notably, high-completeness MAG affiliated with the family *Methanomethylicaceae* (class *Methanomethylicia*) was retrieved from the P53 microbial mat (Supplementary Table 22). *Methanomethylicia*, formerly Verstraetearchaeota[74], belongs to phylum Thermoproteota and represents one of the deepest methanogenic lineages outside Euryarchaeota. Genomic surveys have repeatedly recovered *mcr* genes in this lineage[75,76], and the recent isolation of Candidatus *Methanosuratincola verstraetei LCB70* from a Yellowstone hot spring provided experimental proof of methyl-reducing, hydrogenotrophic methanogenesis within the group[77]. Phylogenetic analysis of cofactor F_{430}

Table 4 | Taxonomic classification and metabolic capabilities of high-quality metagenome-assembled genomes (MAGs) across hydrothermal pools from Lirima

Taxonomy		Pool						Metabolic Route			Total Dereplicated MAGs
		P42		P53		P60		Methanogenesis	Sulfate reduction	Sulfite reduction	
Domain	Phylum	S	M	S	M	S	M	R1	R4	R5 to R6	
Archaea	Asgardarchaeota	✓	X	X	X	X	X	0	1	0	1
	Thermoproteota	X	X	✓	✓	X	X	1	2	0	3
Bacteria	Acidobacteriota	✓	X	✓	✓	✓	✓	0	7	0	7
	Actinomycetota	X	X	✓	✓	✓	✓	0	4	0	4
	Arandabacterota	✓	X	X	✓	X	X	0	2	0	2
	Armatimonadota	✓	✓	✓	✓	✓	✓	0	13	0	13
	Bacillota	✓	X	✓	✓	✓	✓	0	8	7	8
	Bacteroidota_A	X	X	X	✓	X	X	0	1	1	1
	Chloroflexota	✓	✓	✓	✓	✓	✓	0	27	7	29
	Cyanobacteriota	X	✓	X	X	X	X	0	3	0	3
	Desulfobacterota	✓	✓	✓	✓	✓	✓	0	13	12	15
	Nitrospirota	✓	X	X	X	X	X	0	1	1	1
	Not assigned	✓	X	X	X	X	X	0	1	0	1
	Planctomycetota	✓	✓	✓	✓	✓	✓	0	10	0	10
	Pseudomonadota	✓	✓	X	✓	X	X	0	4	4	4
	Verrucomicrobiota	✓	X	X	X	X	X	0	1	0	1

Distribution of phylogenetic groups and functional capacities for methanogenesis (R1), sulfate reduction (R4), and sulfite reduction (R5-R6) detected in sediment (S) and microbial mat (M) samples (in triplicates) from pools P42, P53, and P60.

Checkmarks (✓) indicate phylum presence; crosses (X) indicate absence. Numbers represent counts of dereplicated metagenome-assembled genomes harboring complete or near-complete marker gene sets for the specified metabolic pathways. A total of 103 dereplicated bins possessed methanogenic, sulfate reduction, or sulfite reduction capabilities from 182 total dereplicated high-quality metagenome-assembled genomes derived from 340 initial assemblies across triplicate samples.

biosynthesis proteins further suggests that methanogenic capacity predates the divergence of the TACK superphylum and Euryarchaeota, indicating that the last common ancestor of Archaea may already have possessed versatile methane metabolisms[78].

Immediately above the ECN, dereplicated MAGs taxonomic composition is dominated by sulfate-reducing lineages. Both *aprA* (adenosine-5′-phosphosulfate reductase) and *dsrAB* (dissimilatory sulfite reductase)-encoding genes, the two canonical markers for sulfate reduction[79], are abundant in these assemblies. This metabolic transition is consistent with ecological studies showing that sulfate-reducing prokaryotes out-compete methanogens for molecular hydrogen under anoxic conditions when sulfate is available[80,81]. Thermodynamic affinities calculated for sulfite reduction (R5–R6) are weakly negative (from -1.6×10^{-2} to -7.1×10^{-4} kcal mol^{-1} e^{-}; Supplementary Table 7), implying that only minimal activation energy is required in-situ, which agrees with the high frequency of dsrAB-positive MAGs.

Several sulfate-reducing bins belong to the Armatimonadota phylum, specifically to classes HRBIN16 and HRBIN17 (Supplementary Table 22). Armatimonadota, first recognized as candidate division OP10 in Yellowstone, has recently emerged as a metabolically versatile group with members capable of chemolithotrophic oxidation of hydrogen, sulfur or iron[82,83].

The HRBIN16 MAGs from Lirima also carry genes for iron oxidation and exhibit genomic potential for sulfate reduction (Supplementary Table 22), exhibiting genomic potential for sulfate reduction. HRBIN17 bins show analogous traits, with genomes encoding *dsrAB* and harboring iron-reduction modules (Supplementary Table 22). Similar HRBIN16-related taxa are among the most transcriptionally active heterotrophs in Yellowstone phototrophic mats[84], underscoring their ecological importance in geothermal habitats. Their occurrence at 4000 m a.s.l. indicates successful adaptation to lowered atmospheric pressure and altered gas solubility, broadening the known environmental range of this phylum.

The combined evidence from thermodynamic modelling, functional potential and lineage-specific phylogeny substantiates the ECN as a critical ecological boundary. Below the ECN, microorganisms with complete methanogenic pathways coincide with high ^{3}H-leucine incorporation and elevated sedimentary C/S ratios, indicating carbon-centered metabolism and vigorous biosynthesis. Above 64 °C ^{3}H-leucine uptake collapses, C/S ratios drop below one and the community genetic repertoire shifts towards sulfate and sulfite reduction. These congruent functional, elemental and genomic signatures demonstrate that the ECN delineates a fundamental transition in energy acquisition and biogeochemical cycling within this high-altitude hydrothermal ecosystem.

To provide independent validation of metagenome-assembled genome-derived metabolic inferences and circumvent potential limitations associated with genome assembly and binning procedures, we conducted direct quantification of functional marker genes from unassembled metagenomic reads (Supplementary Table 23). Read-mapping analysis of methyl-coenzyme M reductase, dissimilatory sulfite reductase, and associated functional genes substantiated the metabolic transitions inferred from reconstructed genomes. Methanogenic gene coverage remained consistently low across samples, achieving detectable levels exclusively in P53 sediment samples with maximum coverage of 0.68%, corroborating the restricted distribution of methanogenic metagenome-assembled genomes. Conversely, sulfate reduction genes exhibited widespread distribution with markedly elevated coverage in microbial mat samples relative to sediments, reaching maximum values of 81.95%. Iron metabolism genes displayed heterogeneous but substantial coverage patterns across thermal pools, providing additional support for the metabolic versatility observed in Armatimonadota metagenome-assembled genomes.

Implications and future directions

The identification of Energetic Convergence Nodes (ECNs) in the Lirima hydrothermal system establishes a quantitative framework for

understanding thermodynamic constraints on microbial metabolism under extreme conditions. The reproducibility of the 63–64 °C convergence temperature across six independent high-altitude systems (obtained previously by Tassi et al.[7]) demonstrates that ECNs represent fundamental thermodynamic properties rather than site-specific phenomena, validating this framework as a transferable methodology for predicting metabolic transitions in diverse geothermal environments.

Under reduced atmospheric pressure (~0.5–0.6 atm), these environments provide natural analogues for early Earth conditions. The integration of thermodynamic modelling with molecular evidence demonstrates that theoretical energy landscapes translate directly into observable biological responses. Temperature-specific points where different metabolic reactions yield equivalent chemical affinities reveal energetic constraints that shape microbial niche occupancy and potential biosignatures for astrobiological exploration.

The ECN framework provides a complementary perspective to traditional resource availability[85] or metabolic capability[86] studies by revealing how energetic equivalence among competing redox processes influences community composition. Temperature-dependent metabolic trade-offs between carbon and sulfur-based metabolisms could serve as energetic biosignatures when interpreted alongside atmospheric chemistry data from extraterrestrial targets such as Enceladus or Europa.

Future investigations should evaluate the influence of major ionic composition, particularly bicarbonate, nitrate, and chloride concentrations, alongside pH variations in determining redox thermodynamics. This approach may reveal additional ECNs in oxic environments or alternative reaction couples, expanding the framework to encompass diverse biogeochemical cycles. Experimental validation across broader thermal, physicochemical, and geochemical gradients will establish the universality of ECN predictions through systematic surveys of hydrothermal, marine, saline, and freshwater systems worldwide.

Building on the preliminary genomic evidence presented here, ongoing research will expand analysis to comprehensively characterize carbon, nitrogen, and sulfur cycling pathways, analyzing gene presence and expression alongside corresponding KEGG modules. This approach will enable prediction of microbial community composition based solely on environmental energy budgets. The biotechnological potential of ECN-defined communities warrants investigation, particularly regarding environmental controls on biosynthetic gene cluster expression[22].

Our validation of chemical-affinity calculations confirms that combining field-measured geochemical composition with established speciation software provides reliable theoretical estimates of available energy in complex natural solutions. This methodology offers a tool for predicting energy budgets in diverse hydrothermal environments, enabling systematic surveys of energetic landscapes across planetary scales.

The presence of deep-branching methanogenic lineages close below the ECN and diverse sulfate-reducing taxa above it suggests that energetic convergence zones may have served as evolutionary crucibles for metabolic innovation during early Earth history, providing insights into Archaean biogeochemistry under similar reduced atmospheric pressures.

In conclusion, by quantitatively linking temperature, chemical energetics, and microbial adaptation in a pressure-constrained hydrothermal setting, our work establishes a foundation for thermodynamically informed biosignature detection. The ECN framework offers a systematic approach for predicting microbial community structure across extreme environments, guiding the search for life in analogous extraterrestrial environments.

Methods

Study site

The Lirima hydrothermal system (Fig. 1a, b) is situated in northern Chile's Tarapacá Region at 4000 meters above sea level (m a.s.l.), 25 kilometers southwest of the Sillajguay volcanic chain. The study area is characterized by the occurrence of sinter deposits[7] and thermal pools exhibiting bubbling gases (Fig. 1c). These features are encompassed within the Lirima graben, the main geological structure at the site[7].

Six pools, first reported by Pérez et al.[8], were selected for sampling based on their microbiological structures and conspicuous microbial mats, visible to the naked eye only at temperatures between 42 and 60 °C (Fig. 1d–h). All pools exhibited brown-reddish to greyish lime-grained sediments and showed distinct physical, chemical and biological attributes, reflecting diverse environmental conditions:

P42 (19°50'39.4" S, 68°54'24.4" W; Fig. 1d) is a shallow pool of 0.2 m depth, characterized by brown to reddish sediments and a thin orange microbial mat on its surface.

P53 (19°50'39.3" S, 68°54'24.3" W; Fig. 1d), adjacent and connected to P42, is deeper at 1.5 m, displaying low bubbling activity, greyish sediments and notably fewer visible biological structures compared to P42.

P55 (19°50'34.6" S, 68°54'22.4" W; Fig. 1e) is a shallow pool with depths ranging from 0.2 to 0.4 m. This pool features densely colored, substantial microbial mats exhibiting a diverse palette of greens, oranges, browns, yellows and purples, entirely covering the pool's surface.

P60 (19°50'38.9" S, 68°54'23.8" W; Fig. 1f) varies in depth from 0.5 m to 2.0 m. It features slow bottom bubbling, greyish to light blue sediments and no visible biological structures.

P63 (19°50'37.9" S, 68°54'23.4" W; Fig. 1g) is a shallow pool of 0.3 m depth, exhibiting the strongest bubbling activity through three distinct emission points and greyish lime-grained sediments.

P72 (19°50'37.0" S, 68°54'23.8" W; Fig. 1h), the hottest and deepest pool studied, reaches 3.5 m depth and is characterized by dark greyish sediments with no visible microbial mats.

Physical and chemical parameters in water

Physical and chemical parameters were measured in triplicate ($n = 18$ measurements) at each thermal pool using a Hanna-HI98194 multiparameter probe. Measurements were taken at 10 cm below the water surface to ensure spatial consistency. Temperature readings showed ±0.2 °C precision across the range 53–75 °C; whilst pH values maintained ±0.1 unit precision between pH 6.2–7.3. Electrical conductivity measurements ranged from 1730 to 2130 μS cm^{-1} with ±0.04 mS cm^{-1} precision. The high-altitude location (>4000 m a.s.l.) required specific calibration protocols to account for reduced atmospheric pressure (~0.6 atm), which influences chemical equilibria and gas solubility.

Water sampling

Water samples were collected in triplicate from each pool following previously established protocols[87]. At each sampling point, we filtered two 50 mL aliquots through 0.45 μm cellulose acetate syringe filters. Samples were stored in high-clarity polypropylene conical tubes, pre-cleaned with 10% HCl (48 h) and rinsed four times with Milli-Q water to prevent contamination. For major cation and trace element analyses, samples were acidified to pH ~2 with ultra-pure HNO_3 to prevent calcite precipitation. All samples were stored at 4 °C in darkness from collection through analysis to maintain chemical integrity.

Water geochemical analysis

Anion analysis included HCO_3^- and Cl^- determination by HCl and $AgNO_3$ (Mohr) titration, respectively, while SO_4^{2-} was quantified using the EPA-NERL 375.3 gravimetric method[88]. Major cations (Ca^{2+}, Mg^{2+}, K^+, Na^+, Li^+) and hydrothermal trace elements (As, Cu, Fe, Mn, Sb, Zn) were measured using a PerkinElmer DV7000 ICP-OES at the Centro de Investigación Tecnológica del Agua y Sustentabilidad en el Desierto (CEITSAZA), Universidad Católica del Norte (UCN).

Quality control measures ensure data reliability through multiple validation steps. Element measurements-maintained calibration curves with $R^2 > 0.9$, supported by method blanks and analytical duplicates. Ionic balance calculations confirmed water chemistry data validity, with errors <5% across all samples. Regular analysis of certified reference materials verified measurement accuracy throughout the analytical sequence.

Sediment sampling and pre-processing

Sediment samples were collected beneath the water column using plastic shovels pre-cleaned with 10% HCl (48 h). We sampled the upper 3 cm sediment layer across a 1 m^2 area[87]. Samples were stored in sterile polyethylene bags at 4 °C in darkness until laboratory processing. Sediments were dried at 40 °C in a Binder ED53 gravity convection dryer and homogenized using an agate mortar.

Geochemical analysis of sediment samples

Sediments were digested samples using reverse aqua regia (4 mL ultra-pure HCl, 12 mL ultra-pure HNO_3, 300 mg dried sediment) following EPA Method 3051A[89]. Digestion was performed using a Milestone ETHOS EASY microwave system at CEITSAZA facilities. The solutions were filtered through grade 5 qualitative paper and diluted to 100 mL with Milli-Q water. We quantified trace elements (Sb, As, Cu, Fe, Mn, Zn) using a PerkinElmer DV7000 ICP-OES. Analytical quality was verified through calibration curves, blanks and duplicates, maintaining $R^2 > 0.9$ for all measurements.

Dissolved gases in water

Water samples were collected for dissolved gases measurements (CH_4 and CO_2), in triplicate on 21–22 January 2022 using 20 mL borosilicate vials. Samples were preserved with 50 µL saturated $HgCl_2$, sealed without air bubbles and stored inverted at room temperature (25 °C) in darkness until analysis at the Laboratorio de Biogeoquímica de Gases de Efecto Invernadero (LABGEI), Pontificia Universidad Católica de Valparaíso (PUCV, Chile). $HgCl_2$, was selected as a preservative based on its established use in environmental samples to inhibit microbial activity. While some thermophilic microorganisms can develop mercury resistance, the high concentration used (50 µL saturated solution) ensures effective preservation for the targeted gas analysis. Samples were processed promptly to minimize any potential influence of mercury-resistant microorganisms.

Gas analysis employed the headspace equilibration method[90] using ultra-pure He. We analyzed the equilibrated headspace using a Shimadzu GC-2014 gas chromatograph equipped with a methanizer for CO_2 conversion to CH_4 and flame ionization detector (FID) for CH_4 determination. Concentrations were calculated using a three-point calibration curve with He, air and certified Scotty gas mixture (Air Liquid Co.; 600 ppm CO_2, 5 ppm CH_4).

While hydrogen (H_2) is an important potential energy source in hydrothermal systems, direct field measurement presented technical challenges due to several factors. The remote high-altitude field site (4000 m elevation) created logistical limitations for transporting specialized gas analysis equipment. H_2 is among the most difficult dissolved gases to accurately sample and preserve in hydrothermal environments due to its high diffusivity and rapid biological consumption[19].

Instead, we followed established practice for geothermal systems by deriving H_2 activities from measured redox indicators. For thermodynamic calculations, H_2 activities were modelled through redox equilibria in PHREEQC[30] using the measured parameters of temperature, pH, ORP, aqueous geochemistry and dissolved gases. This approach has been validated in comparable geothermal systems where modelled activities derived from field measurements[47,48]. Furthermore, our thermodynamic analysis includes parallel calculations with and without measured CO_2 and CH_4 gases to test sensitivity, confirming that the calculated ECNs positions remain robust despite inherent uncertainties in H_2 activity estimation.

Organic matter $\delta^{13}C_{(VPDB)}$ and $\delta^{34}S_{(VCDT)}$ isotopes in sediments

Sediment samples (15 g) were preserved from each pool at −20 °C in sterile polyethylene bags for processing at the Fish and Aquatic Ecology and Stable Isotope Ecology Laboratory, Universidad de Antofagasta. Samples were lyophilized at −84 °C under vacuum for 48–72 h using a LABCONCO FreeZone Plus Cascade freeze dryer, then homogenized using 2 mm steel beads. For $\delta^{13}C_{(VPDB)}$ analysis, we removed inorganic carbon using 2 N HCl in 2 mL Eppendorf tubes, followed by centrifugation relative centrifugal force (RCF) of 460 × g (2 min) and two Milli-Q water rinses. Sulfur isotope analysis used untreated sediments. We weighed 8.00 ± 0.10 mg of processed sediment into tin capsules using a Mettler Toledo XS 3DU microbalance (Greifensee, Switzerland; repeatability ±0.0008 mg).

Carbon and sulfur elemental percentages and stable isotope ratios ($\delta^{13}C_{(VPDB)}$, $\delta^{34}S_{(VCDT)}$) were measured at the Universidad de Antofagasta Stable Isotope Facility using a Pyrocube elemental analyzer coupled to a visION continuous-flow isotope ratio mass spectrometer (Elementar, Langenselbold, Germany). We report stable isotope ratios in δ notation (‰) relative to Vienna Pee Dee Belemnite (VPDB) for carbon and Vienna Canyon Diablo Troilite (VCDT) for sulfur, calculated as:

$$\delta = \left(R_{Sample}/R_{Standard} - 1\right) \quad (1)$$

where R represents $^{13}C/^{12}C$ or $^{34}S/^{32}S$ ratios.

Analysis used multi-point calibration through ionOS software v4.1.005 (Elementar) with certified standards (USGS40 and USGS41a for carbon; IAEA-SO-5, IAEA-SO-6, and IAEA-S2 for sulfur). Triplicate analyses-maintained errors within ±0.07‰ for $\delta^{13}C_{(VPDB)}$ and ±0.14‰ for $\delta^{34}S_{(VCDT)}$. The high-altitude sampling environment required specific consideration due to isotopic fractionation effects under reduced atmospheric pressure, providing insights into microbial metabolic pathways in the sediments.

Thermodynamic calculations of anoxic inorganic reactions

Thermodynamic calculations focused on 10 inorganic carbon and sulfur reactions under anoxic conditions (Table 3), representing key metabolic pathways in hydrothermal systems. While oxygen-dependent processes occur in these environments, the analysis specifically examined anaerobic reactions to understand energy availability for chemolithotrophic metabolism.

Elemental sulfur reduction, though potentially relevant in some hydrothermal systems, was not included in our analysis due to the focus on reactions involving the predominant measured species (SO_4^{2-}, CO_2, CH_4). Future studies incorporating direct S^0 measurements and targeted metabolic marker genes could further assess its potential role in these systems.

Chemical activities were simulated in PHREEQC v3.0[30] using the *llnl.dat* geothermal database. Two complementary models were run on 1 kg of fluid: one constrained by measured temperature, pH, ORP and aqueous geochemistry (at ~0.6 atm[9]) and the other additionally incorporating in-situ CO_2 and CH_4 dissolved gases. Both reproduce the undersaturated state of CO_2(g), CH_4(g), H_2(g) and H_2S(g) (Supplementary Table 3) and yield saturation indices (SI) and activities (a) for all relevant species. H_2 and H_2S activities derive from PHREEQC speciation[30], following standard protocols for geothermal fluids[32]. The close agreement (ΔECN < 1 °C) between affinities computed with and without CO_2 and CH_4 gases confirms that this approach reliably estimates available energy from solution-only chemistry (Supplementary Tables 6–8).

Chemical affinities (A_r) for ten inorganic anaerobic reactions (Table 3) were calculated using:

$$A_r = R^*T^*\ln\left(K_r/Q_r\right) \quad (2)$$

where R represents the gas constant, T the field-measured temperature (in Kelvin), K_r the equilibrium constant and Q_r the reaction product of activities, derived from PHREEQC-simulated activities and reaction stoichiometry.

The equilibrium constant (K_r) was determined through:

$$K_r = e^{-\Delta G^\circ r/R^*T} \quad (3)$$

where ΔG°r values were interpolated via cubic regression ($R^2 > 0.99$, $p < 0.05$) of published data that includes a temperature range between 2 and 200° C[15]. Field temperatures (53–75 °C) fell within this calibration range. Chemical affinities, initially calculated in J mol^{-1}, were converted to kcal

mol^{-1} (factor: 0.00023906) and normalized by electron transfer (Table 3) to obtain kcal mol^{-1} e^-.

Energy density (E_r) calculations (Supplementary Table 12) incorporated limiting reactants (Supplementary Table 14) for each reaction (Table 3):

$$E_r = A_r^* e - {}^* a_{(\text{limiting reactant})} / \text{stoichiometric coefficient}_{(\text{limiting reactant})} \quad (4)$$

where A_r represents energy in J mol^{-1}, e^- the electrons transferred and (a) the activity of the limiting reactant, identified by determining the minimum ratio of PHREEQC-simulated activity to stoichiometric coefficient. Results are expressed in J kgH_2O^{-1}.

Gas saturation indices were determined through:

$$SI = \log(IAP/Ksp) \quad (5)$$

where IAP represents ion activity product and Ksp the temperature-dependent solubility. For simulations without measured gases, PHREEQC predicted theoretical concentrations of CO, H_2, H_2S, S_2 and SO_2 based on solution chemistry and redox conditions. For simulations incorporating field data, measured CO_2 and CH_4 were used to validate the model, whilst concentrations of other gases were theoretically derived. In both cases, gas equilibrium states followed Henry's law:

$$C = KH(T)^* P \quad (6)$$

where C denotes dissolved gas concentration, P the partial pressure and KH(T) the temperature-dependent Henry's constant. Negative SI values indicate undersaturation potential, while positive values suggest gas exsolution tendency.

^{3}H-Leucine incorporation experiment

Heterotrophic bacterial production was measured using ^{3}H-leucine incorporation across a thermal gradient in hydrothermal pools (P42, P53, P55 and P72). Water samples were collected directly from pools and ^{3}H-leucine (Perkin Elmer; specific activity 100 Ci $mmol^{-1}$) was added to achieve a final concentration of 10 nM. Triplicate 5 mL samples were incubated in polyethylene bags in the hydrothermal pools (i.e., in-situ temperature) under full solar irradiation for 4 h centered around solar noon. Incorporation reactions were terminated with trichloroacetic acid (TCA) to a final concentration of 5% (v/v), and samples were processed following established protocols[91]. Biological replicates ($n = 3$) were conducted at each temperature with triplicate measurements to ensure statistical robustness.

Metagenomic Sequencing and Analysis

Genomic DNA was extracted from 0.25 g of each sediment or microbial-mat subsample from P42, P53 and P60, using the DNeasy PowerSoil kit (Qiagen, Hilden, Germany) following the manufacturer's protocol. Integrity was confirmed on a one-per-cent agarose gel, and concentrations were determined with a Qubit 2.0 fluorometer using the double-stranded-DNA High-Sensitivity assay (Thermo Fisher Scientific, Waltham, USA).

Indexed paired-end libraries (2 × 150 bp) were prepared with the Nextera XT kit (Illumina, San Diego, USA) and sequenced on an Illumina NextSeq 1000 at the AustralOmics facility (Valdivia, Chile). Raw reads were inspected with FastQC v0.12.1 (https://www.bioinformatics.babraham.ac.uk/projects/fastqc/). Adapter trimming and quality filtering were performed with fastp[92,93] v0.24.0 using automatic paired-end adapter detection and the options --cut_front --cut_tail --cut_mean_quality 15 --length_required 15 (fastp --detect_adapter_for_pe --cut_front --cut_tail --cut_mean_quality 15 --length_required 15).

The trimmed reads were then aligned against the Illumina PhiX174 control genome (archive PhiX_NCBI_1993-04-28.tar.gz) with bowtie2-align-s[94] v2.5.4 to remove laboratory spike-in contamination. The alignment command was bowtie2 -x PhiX_NCBI_1993-04-28 -1 < R1_trimmed.fastq.gz > -2 < R2_trimmed.fastq.gz > --un-conc-gz <clean_prefix > -S <phix.sam > -p 32. Read pairs that did not map to PhiX (--un-conc-gz) were retained as the final high-quality dataset for de-novo assembly and metagenomic binning. The sequences were deposited in DDBJ/ENA/GenBank databases under BioProject accession number PRJNA1125025.

Shotgun metagenomes from eighteen samples (three pools, each analyzed in sediment and mat matrices and processed in triplicate) were assembled de-novo with metaSPAdes[95] v3.15.3 in metagenomic mode. Assembly statistics (total length, N50, largest contig and GC content) were evaluated with QUAST[96] v5.0.2.

Read recruitment was performed with Bowtie2 v2.5.4 after indexing each scaffold set, and coverage profiles were calculated with jgi_summarize_bam_contig_depths. Genome bins were generated independently with MetaBAT2[97] v2.15 and MaxBin2[98] v2.2.4, then reconciled with DAS Tool[99] v1.1.5, which selects the optimum non-redundant bin set based on single-copy marker scores.

Bin quality was determined with CheckM[100] v1.2.2. Genomes exhibiting ≥ 90% completeness and ≤ 5% contamination were designated high-quality; those with ≥ 50% completeness and ≤ 10% contamination were designated medium-quality; all others were discarded. High-quality bins recovered from the three technical replicates of each pool–matrix combination were dereplicated with dRep[101] v3.5.0 using the ANImf algorithm at a 90% average nucleotide identity threshold, yielding a non-redundant genome catalogue.

Taxonomic placements were assigned using the standard classification workflow in GTDB-Tk[102–109] v2.4.1 against GTDB database[110] release R226. Whilst taxonomic assignments achieved genus-level resolution for several MAGs, family-level classification was adopted as the primary taxonomic rank for ecological analysis, as the most abundant lineages associated with methanogenesis and sulfate/sulfite reduction were consistently classified to this level, enabling comparative analysis across metabolic groups. Metabolic potential was annotated with METABOLIC-C[111] v4.0, which was applied both to reconstructed metagenome-assembled genomes for pathway and energy-budget analyses and to unassembled metagenomic reads for direct coverage estimation of key functional genes.

Statistical analysis

Statistical analyses were conducted in R (v4.2.0) using a multi-tiered approach to examine relationships between physicochemical variables and validate thermodynamic calculations. Non-parametric Kendall's τ tests and cubic regression models were employed to characterize the relationships between temperature and both chemical affinities and isotopic/elemental proxies. Cubic fits were selected over linear or quadratic alternatives by minimizing the Akaike Information Criterion (AIC) and Bayesian Information Criterion (BIC) values (Supplementary Tables 10 and 15). This selection is theoretically justified because standard Gibbs free energy values ($\Delta G°_{std}$) exhibits third-order temperature dependence, which accurately represents thermodynamic properties across wide temperature ranges[15,112]. This ensured that inflection points corresponding to our ECNs were captured. Kendall's τ analyses (Supplementary Table 9) provide non-parametric confirmation of these non-linear trends (Supplementary Table 10). Significance thresholds were set at $p \leq 0.05$, with cubic fits requiring $R^2 > 0.5$ for inclusion in subsequent analyses (Supplementary Tables 2, 9, 16 and 20). Data manipulation and visualization employed tidyverse and ggplot2 packages, with correlation matrices visualized through corrplot and RColorBrewer.

Chemical affinity and energy density calculations underwent error propagation analysis using a bootstrap approach (boot package, 2000 iterations). This process incorporated measured dissolved gases scenarios (wG) and theoretical calculations without measured gases (woG), yielding uncertainty estimates and 95% confidence intervals reaction pathways (R1-R10, Table 3). Thermodynamic convergence points were identified through numerical root-finding of cubic-fitted chemical affinity differences (rootSolve package). Bootstrap validation provided intersection temperature estimates with associated uncertainties below 6.2%, establishing statistically robust metabolic transition points.

Comparative analyses between wG and woG scenarios for chemical affinities (Supplementary Table 8) and energy densities (Supplementary Table 13) employed one-way ANOVA (car package), requiring minimum sample sizes of $n = 3$ per group. ANOVA assumptions were validated through Shapiro-Wilk tests for normality (stats package) and Levene's test for variance homogeneity (car package). Temperature-dependent trends in isotopic data ($\delta^{13}C_{(VPDB)}$, $\delta^{34}S_{(VCDT)}$) and elemental ratios (C/S) were assessed through both Kendall correlations and cubic regressions, maintaining consistent significance criteria ($p \leq 0.05$).

The integrated statistical framework quantified uncertainties in chemical affinities (mean SE < 1%), energetic convergence temperatures (63.8–64.0 °C ± 0.2%), establishing robust validation of observed thermodynamic patterns and metabolic transitions across thermal gradients.

Ethical approval and consent to participate

This study involved collaborative partnerships with local Chilean researchers and institutions throughout all phases of research. The first author is a member of the Quechua indigenous community native to the northern Chilean study region, ensuring indigenous perspectives and local knowledge integration. Research was conducted with appropriate community permissions and local scientific leadership, following ethical practices for studies in indigenous territories.

Reporting summary

Further information on research design is available in the Nature Portfolio Reporting Summary linked to this article.

Data availability

The data supporting the conclusions of this study are provided within the manuscript and accompanying supplementary material. Metagenomic raw reads and all 182 dereplicated metagenome-assembled genomes have been deposited in the DDBJ/ENA/GenBank databases under BioProject accession number PRJNA1125025 and PRJNA1303110, respectively. Source data underlying all figures (Supplementary Tables 1, 7, 18, and 21) are available in Figshare repository under https://doi.org/10.6084/m9.figshare.29930546. All datasets are publicly accessible without restrictions.

Received: 10 May 2025; Accepted: 22 September 2025;
Published online: 11 November 2025

References

1. Kasting, J. F. Earth's early atmosphere. *Science* **259**, 920–926 (1993).
2. Mercury, L., Azaroual, M., Zeyen, H. & Tardy, Y. Thermodynamic properties of solutions in metastable systems under negative or positive pressures. *Geochimica et. Cosmochimica Acta* **67**, 1769–1785 (2003).
3. Som, S. M. et al. Earth's air pressure 2.7 billion years ago constrained to less than half of modern levels. *Nat. Geosci.* **9**, 448–451 (2016).
4. Miller, S. L. & Urey, H. C. Organic compound synthesis on the primitive Earth: Several questions about the origin of life have been answered, but much remains to be studied. *Science* **130**, 245–251 (1959).
5. Catling, D. C. & Zahnle, K. J. The archean atmosphere. *Sci. Adv.* **6**, eaax1420 (2020).
6. Sajeev, Y. Prebiotic chemical origin of biomolecular complementarity. *Commun. Chem.* **6**, 259 (2023).
7. Tassi, F. et al. Fluid geochemistry of hydrothermal systems in the Arica-Parinacota, Tarapacá and Antofagasta regions (northern Chile). *J. Volcanol. Geotherm. Res.* **192**, 1–15 (2010).
8. Pérez, V. et al. Aquatic thermal reservoirs of microbial life in a remote and extreme high andean hydrothermal system. *Microorganisms* **8**, 208 (2020).
9. Paquis, P. et al. Short-term characterisation of climatic-environmental variables and microbial community diversity in a high-altitude Andean wetland (Salar de Huasco, Chile). *Sci. Total Environ.* **859**, 160291 (2023).
10. Molina, V. et al. Greenhouse gases and biogeochemical diel fluctuations in a high-altitude wetland. *Sci. Total Environ.* **768**, 144370 (2021).
11. Shock, E. L., Holland, M., Amend, J. P., Osburn, G. R. & Fischer, T. P. Quantifying inorganic sources of geochemical energy in hydrothermal ecosystems, Yellowstone National Park, USA. *Geochimica et. Cosmochimica Acta* **74**, 4005–4043 (2010).
12. González-Cabaleiro, R., Ofițeru, I. D., Lema, J. M. & Rodríguez, J. Microbial catabolic activities are naturally selected by metabolic energy harvest rate. *ISME J.* **9**, 2630–2641 (2015).
13. Havig, J. R., Hamilton, T. L., Bachan, A. & Kump, L. R. Sulfur and carbon isotopic evidence for metabolic pathway evolution and a four-stepped Earth system progression across the Archean and Paleoproterozoic. *Earth-Sci. Rev.* **174**, 1–21 (2017).
14. Lewis, G. N., & Randall, M. Thermodynamics and the free energy of chemical substances. McGraw-Hill (1923).
15. Amend, J. P. & Shock, E. L. Energetics of overall metabolic reactions of thermophilic and hyperthermophilic Archaea and Bacteria. *FEMS Microbiol. Rev.* **25**, 175–243 (2001).
16. Sánchez-García, L. et al. Fingerprinting molecular and isotopic biosignatures on different hydrothermal scenarios of Iceland, an acidic and sulfur-rich Mars analog. *Sci. Rep.* **10**, 21196 (2020).
17. Calabrese, S., Chakrawal, A., Manzoni, S. & Van Cappellen, P. Energetic scaling in microbial growth. *Proc. Natl. Acad. Sci.* **118**, e2107668118 (2021).
18. Montaño López, J., Duran, L. & Avalos, J. L. Physiological limitations and opportunities in microbial metabolic engineering. *Nat. Rev. Microbiol.* **20**, 35–48 (2022).
19. Seewald, J. S. Detecting molecular hydrogen on Enceladus. *Science* **356**, 132–133 (2017).
20. Peter, J. S., Nordheim, T. A. & Hand, K. P. Detection of HCN and diverse redox chemistry in the plume of Enceladus. *Nat. Astron.* **8**, 164–173 (2024).
21. Pandey, S. et al. Ladakh: diverse, high-altitude extreme environments for off-earth analogue and astrobiology research. *Int. J. Astrobiol.* **19**, 78–98 (2020).
22. Pardo-Esté, C. et al. Secondary metabolites with antimicrobial activity produced by thermophilic bacteria from a high-altitude hydrothermal system. *Front. Microbiol.* **15**, 1477458 (2024).
23. Das, S. & Adhya, T. K. Dynamics of methanogenesis and methanotrophy in tropical paddy soils as influenced by elevated CO_2 and temperature interaction. *Soil Biol. Biochem.* **47**, 36–45 (2012).
24. Bonaiuti, S., Blodau, C. & Knorr, K. H. Evaluating biogeochemical indicators of methanogenic conditions and thermodynamic constraints in peat. *Appl. Geochem.* **114**, 104471 (2020).
25. Zhan, S., Zeng, L., Al-Yaseri, A., Sarmadivaleh, M. & Xie, Q. Geochemical modelling on the role of redox reactions during hydrogen underground storage in porous media. *Int. J. Hydrog. Energy* **50**, 19–35 (2024).
26. Lu, P., Zhang, G., Apps, J. & Zhu, C. Comparison of thermodynamic data files for PHREEQC. *Earth-Sci. Rev.* **225**, 103888 (2022).
27. Dodangoda, C. Quantification of hydrogen depletion and mineral reactivity in underground hydrogen storage reservoirs. *Gas. Sci. Eng.* **126**, 205318 (2024).
28. Zou, J. et al. Rewetting global wetlands effectively reduces major greenhouse gas emissions. *Nat. Geosci.* **15**, 627–632 (2022).
29. Bao, T., Jia, G. & Xu, X. Weakening greenhouse gas sink of pristine wetlands under warming. *Nat. Clim. Change* **13**, 462–469 (2023).
30. Parkhurst, D. L. & Appelo, C. A. J. Description of input and examples for PHREEQC version 3—a computer program for speciation, batch-reaction, one-dimensional tra. (2013).

31. Hörbrand, T., Baumann, T. & Moog, H. C. Validation of hydrogeochemical databases for problems in deep geothermal energy. *Geotherm. Energy* **6**, 20 (2018).
32. Josephat, S., Stefánsson, A. & Óskarsson, F. Major and Trace Elements Geochemistry of Natural Waters at Mt. Meru Volcano, Tanzania.
33. Hu, Z. & Gao, S. Upper crustal abundances of trace elements: A revision and update. *Chem. Geol.* **253**, 205–221 (2008).
34. Kappler, A. et al. An evolving view on biogeochemical cycling of iron. *Nat. Rev. Microbiol.* **19**, 360–374 (2021).
35. He, Z. et al. Microbiological and environmental significance of metal-dependent anaerobic oxidation of methane. *Sci. Total Environ.* **610**, 759–768 (2018).
36. Beulig, F., Røy, H., McGlynn, S. E. & Jørgensen, B. B. Cryptic CH4 cycling in the sulfate–methane transition of marine sediments apparently mediated by ANME-1 archaea. *ISME J.* **13**, 250–262 (2019).
37. Shi, L. D. et al. Coupled anaerobic methane oxidation and reductive arsenic mobilization in wetland soils. *Nat. Geosci.* **13**, 799–805 (2020).
38. Zhu, J. et al. Insight of bacteria and archaea in Feammox community enriched from different soils. *Environ. Res.* **203**, 111802 (2022).
39. González, H. et al. Ammonium and organic carbon co-removal under Feammox heterotrophic conditions at low Fe^{3+} concentrations. *Bioresource Technol.* **434**, 132750 (2025).
40. Boyd, P. W., Ellwood, M. J., Boyd, P. W. & Ellwood, M. J. The biogeochemical cycle of iron in the ocean. *Nat. Geosci.* **3**, 675–682 (2010).
41. Tagliabue, A. et al. The integral role of iron in ocean biogeochemistry. *Nature* **543**, 51–59 (2017).
42. Ninin, J. M. L., Mori, A. H., Pausch, J. & Planer-Friedrich, B. Long-term paddy use influences response of methane production, arsenic mobility and speciation to future higher temperatures. *Sci. Total Environ.* **943**, 173793 (2024).
43. Canfield, D. E. Isotope fractionation by natural populations of sulfate-reducing bacteria. *Geochimica et. Cosmochimica Acta* **65**, 1117–1124 (2001).
44. Farquhar, J. & Wing, B. A. Multiple sulfur isotopes and the evolution of the atmosphere. *Earth Planet. Sci. Lett.* **213**, 1–13 (2003).
45. Lamb, A. L., Chenery, C. A., Madgwick, R. & Evans, J. A. Wet feet: developing sulfur isotope provenance methods to identify wetland inhabitants. *R. Soc. Open Sci.* **10**, 230391 (2023).
46. Spycher, N. F. & Reed, M. H. Fugacity coefficients of H_2, CO_2, CH_4, H_2O, and of H_2O-CO_2-CH_4 mixtures: A virial equation treatment for moderate pressures and temperatures applicable to calculations of hydrothermal boiling. *Geochimica et. Cosmochimica Acta* **52**, 739–749 (1988).
47. Stefánsson, A., Arnórsson, S. & Sveinbjörnsdóttir, ÁE. Redox reactions and potentials in natural waters at disequilibrium. *Chem. Geol.* **221**, 289–311 (2005).
48. Kaasalainen, H. & Stefánsson, A. Sulfur speciation in natural hydrothermal waters, Iceland. *Geochimica et. Cosmochimica Acta* **75**, 2777–2791 (2011).
49. Reeves, E. P. & Seewald, J. S. Hydrothermal carbon reduction in the absence of minerals. *Geochimica et. Cosmochimica Acta* **381**, 60–74 (2024).
50. Blouet, J. P., Arndt, S., Imbert, P. & Regnier, P. Are seep carbonates quantitative proxies of CH4 leakage? Modeling the influence of sulfate reduction and anaerobic oxidation of methane on pH and carbonate precipitation. *Chem. Geol.* **577**, 120254 (2021).
51. Akunna, J. C., Bernet, N. & Moletta, R. Effect of nitrate on methanogenesis at low redox potential. *Environ. Technol.* **19**, 1249–1254 (1998).
52. Appelo, C. A. J., & Postma, D. Geochemistry, groundwater and pollution. CRC press. (2004)
53. Ellis, A. J. & Mahon, W. A. J. Chemistry and geothermal systems. (1977).
54. Kharaka, Y. K. & Mariner, R. H. Chemical geothermometers and their application to formation waters from sedimentary basins. In Thermal history of sedimentary basins: methods and case histories (pp. 99-117). New York, NY: Springer New York. (1989)
55. Hayes, J. M. Fractionation of carbon and hydrogen isotopes in biosynthetic processes. *Rev. Mineral. Geochem.* **43**, 225–278 (2001).
56. Galand, P. E., Yrjälä, K. & Conrad, R. Stable carbon isotope fractionation during methanogenesis in three boreal peatland ecosystems. *Biogeosciences* **7**, 3893–3900 (2010).
57. Antler, G., Turchyn, A. V., Ono, S., Sivan, O. & Bosak, T. Combined 34S, 33S and 18O isotope fractionations record different intracellular steps of microbial sulfate reduction. *Geochimica et. Cosmochimica Acta* **203**, 364–380 (2017).
58. Nordstrom, D. K., McCleskey, R. B. & Ball, J. W. Sulfur geochemistry of hydrothermal waters in Yellowstone National Park: IV Acid–sulfate waters. *Appl. Geochem.* **24**, 191–207 (2009).
59. Plugge, C. M., Zhang, W., Scholten, J. C. & Stams, A. J. Metabolic flexibility of sulfate-reducing bacteria. *Front. Microbiol.* **2**, 81 (2011).
60. Hoehler, T. M. & Jørgensen, B. B. Microbial life under extreme energy limitation. *Nat. Rev. Microbiol.* **11**, 83–94 (2013).
61. Ferenci, T. Trade-off mechanisms shaping the diversity of bacteria. *Trends Microbiol.* **24**, 209–223 (2016).
62. Ward, D. M., Castenholz, R. W. & Miller, S. R. Cyanobacteria in geothermal habitats. In Ecology of cyanobacteria II: their diversity in space and time (pp. 39-63). Dordrecht: Springer Netherlands. (2012)
63. Sharp, C. E. et al. Humboldt's spa: microbial diversity is controlled by temperature in geothermal environments. *ISME J.* **8**, 1166–1174 (2014).
64. Cox, A., Shock, E. L. & Havig, J. R. The transition to microbial photosynthesis in hot spring ecosystems. *Chem. Geol.* **280**, 344–351 (2011).
65. Sabath, N., Ferrada, E., Barve, A. & Wagner, A. Growth temperature and genome size in bacteria are negatively correlated, suggesting genomic streamlining during thermal adaptation. *Genome Biol. Evol.* **5**, 966–977 (2013).
66. Kirchman, D., K'nees, E. L. I. Z. A. B. E. T. H. & Hodson, R. Leucine incorporation and its potential as a measure of protein synthesis by bacteria in natural aquatic systems. *Appl. Environ. Microbiol.* **49**, 599–607 (1985).
67. Tibbles, B. J. Effects of temperature on the incorporation of leucine and thymidine by bacterioplankton and bacterial isolates. *Aquat. Microb. Ecol.* **11**, 239–250 (1996).
68. Cathalot, C. et al. Hydrothermal plumes as hotspots for deep-ocean heterotrophic microbial biomass production. *Nat. Commun.* **12**, 6861 (2021).
69. Berner, R. A. & Raiswell, R. C/S method for distinguishing freshwater from marine sedimentary rocks. *Geology* **12**, 365–368 (1984).
70. Goldhaber, M. B. & Kaplan, I. R. Controls and consequences of sulfate reduction rates in recent marine sediments. *Soil Sci.* **119**, 42–55 (1975).
71. Luton, P. E., Wayne, J. M., Sharp, R. J. & Riley, P. W. The mcrA gene as an alternative to 16S rRNA in the phylogenetic analysis of methanogen populations in landfill. *Microbiology* **148**, 3521–3530 (2002).
72. Hua, Z. S. et al. Insights into the ecological roles and evolution of methyl-coenzyme M reductase-containing hot spring Archaea. *Nat. Commun.* **10**, 4574 (2019).
73. Wang, J. et al. Evidence for nontraditional mcr-containing archaea contributing to biological methanogenesis in geothermal springs. *Sci. Adv.* **9**, eadg6004 (2023).

74. Vanwonterghem, I. et al. Methylotrophic methanogenesis discovered in the archaeal phylum Verstraetearchaeota. *Nat. Microbiol.* **1**, 1–9 (2016).
75. Borrel, G. et al. Wide diversity of methane and short-chain alkane metabolisms in uncultured archaea. *Nat. Microbiol.* **4**, 603–613 (2019).
76. Evans, P. N. et al. Methane metabolism in the archaeal phylum Bathyarchaeota revealed by genome-centric metagenomics. *Science* **350**, 434–438 (2015).
77. Kohtz, A. J. et al. Cultivation and visualization of a methanogen of the phylum Thermoproteota. *Nature* **632**, 1118–1123 (2024).
78. Mei, R., Kaneko, M., Imachi, H. & Nobu, M. K. The origin and evolution of methanogenesis and Archaea are intertwined. *PNAS nexus* **2**, pgad023 (2023).
79. Meyer, B. & Kuever, J. Phylogeny of the alpha and beta subunits of the dissimilatory adenosine-5′-phosphosulfate (APS) reductase from sulfate-reducing prokaryotes–origin and evolution of the dissimilatory sulfate-reduction pathway. *Microbiology* **153**, 2026–2044 (2007).
80. Stams, A. J. M. et al. Metabolic interactions in methanogenic and sulfate-reducing bioreactors. *Water Sci. Technol.* **52**, 13–20 (2005).
81. Muyzer, G. & Stams, A. J. The ecology and biotechnology of sulphate-reducing bacteria. *Nat. Rev. Microbiol.* **6**, 441–454 (2008).
82. Kato, S., Masuda, S., Shibata, A., Shirasu, K. & Ohkuma, M. Insights into ecological roles of uncultivated bacteria in Katase hot spring sediment from long-read metagenomics. *Front. Microbiol.* **13**, 1045931 (2022).
83. Nou, N. O. et al. Genome-guided isolation of the hyperthermophilic aerobe Fervidibacter sacchari reveals conserved polysaccharide metabolism in the Armatimonadota. *Nat. Commun.* **15**, 9534 (2024).
84. Shelton, A. N., Yu, F. B., Grossman, A. R. & Bhaya, D. Abundant and active community members respond to diel cycles in hot spring phototrophic mats. *ISME J.* **19**, wraf001 (2025).
85. Feng, X. et al. A checklist for maximizing reproducibility of ecological niche models. *Nat. Ecol. Evolution* **3**, 1382–1395 (2019).
86. Fahimipour, A. K. & Gross, T. Mapping the bacterial metabolic niche space. *Nat. Commun.* **11**, 4887 (2020).
87. Tapia, J., Mukherjee, A., Rodríguez, M. P., Murray, J. & Bhattacharya, P. Role of tectonics and climate on elevated arsenic in fluvial systems: Insights from surface water and sediments along regional transects of Chile. *Environ. Pollut.* **314**, 120151 (2022).
88. EPA, U. Methods for the Chemical Analysis of Water and Wastes (MCAWW)(EPA/600/4-79/020). EPA Method, 375. (1978)
89. EPA, U. Method 3051A (SW-846): microwave assisted acid digestion of sediments, sludges, and oils, revision 1. Washington, DC. (2007)
90. McAuliffe, C. Gas chromatographic determination of solutes by multiple phase equilibrium. *Chem. Technol.* **1**, 46–51 (1971).
91. Hernández, K. et al. Microbial Activity Response to Solar Radiation across Contrasting Environmental Conditions in Salar de Huasco, Northern Chilean Altiplano. *Front. Microbiol*. https://doi.org/10.3389/fmicb.2016.01857 (2016).
92. Chen, S., Zhou, Y., Chen, Y. & Gu, J. fastp: an ultra-fast all-in-one FASTQ preprocessor. *Bioinformatics* **34**, i884–i890 (2018).
93. Chen, S. Ultrafast one-pass FASTQ data preprocessing, quality control, and deduplication using fastp. *Imeta* **2**, e107 (2023).
94. Langmead, B. & Salzberg, S. L. Fast gapped-read alignment with Bowtie 2. *Nat. methods* **9**, 357–359 (2012).
95. Prjibelski, A., Antipov, D., Meleshko, D., Lapidus, A. & Korobeynikov, A. Using SPAdes de novo assembler. *Curr. Protoc. Bioinforma.* **70**, e102 (2020).
96. Mikheenko, A., Saveliev, V., Hirsch, P. & Gurevich, A. WebQUAST: online evaluation of genome assemblies. *Nucleic Acids Res.* **51**, W601–W606 (2023).
97. Kang, D. D. et al. MetaBAT 2: an adaptive binning algorithm for robust and efficient genome reconstruction from metagenome assemblies. *PeerJ* **7**, e7359 (2019).
98. Wu, Y. W., Simmons, B. A. & Singer, S. W. MaxBin 2.0: an automated binning algorithm to recover genomes from multiple metagenomic datasets. *Bioinformatics* **32**, 605–607 (2016).
99. Sieber, C. M. et al. Recovery of genomes from metagenomes via a dereplication, aggregation and scoring strategy. *Nat. Microbiol.* **3**, 836–843 (2018).
100. Parks, D. H., Imelfort, M., Skennerton, C. T., Hugenholtz, P. & Tyson, G. W. CheckM: assessing the quality of microbial genomes recovered from isolates, single cells, and metagenomes. *Genome Res.* **25**, 1043–1055 (2015).
101. Olm, M. R., Brown, C. T., Brooks, B. & Banfield, J. F. dRep: a tool for fast and accurate genomic comparisons that enables improved genome recovery from metagenomes through de-replication. *ISME J.* **11**, 2864–2868 (2017).
102. Price, M. N., Dehal, P. S. & Arkin, A. P. FastTree 2–approximately maximum-likelihood trees for large alignments. *PloS one* **5**, e9490 (2010).
103. Hyatt, D. et al. Prodigal: prokaryotic gene recognition and translation initiation site identification. *BMC Bioinforma.* **11**, 1–11 (2010).
104. Matsen, F. A., Kodner, R. B. & Armbrust, E. V. pplacer: linear time maximum-likelihood and Bayesian phylogenetic placement of sequences onto a fixed reference tree. *BMC Bioinforma.* **11**, 1–16 (2010).
105. Eddy, S. R. Accelerated profile HMM searches. *PLoS computational Biol.* **7**, e1002195 (2011).
106. Ondov, B. D. et al. Mash: fast genome and metagenome distance estimation using MinHash. *Genome Biol.* **17**, 1–14 (2016).
107. Jain, C., Rodriguez-R, L. M., Phillippy, A. M., Konstantinidis, K. T. & Aluru, S. High throughput ANI analysis of 90K prokaryotic genomes reveals clear species boundaries. *Nat. Commun.* **9**, 5114 (2018).
108. Chaumeil, P. A., Mussig, A. J., Hugenholtz, P. & Parks, D. H. GTDB-Tk v2: memory friendly classification with the genome taxonomy database. *Bioinformatics* **38**, 5315–5316 (2022).
109. Shaw, J. & Yu, Y. W. Fast and robust metagenomic sequence comparison through sparse chaining with skani. *Nat. Methods* **20**, 1661–1665 (2023).
110. Parks, D. H. et al. GTDB: an ongoing census of bacterial and archaeal diversity through a phylogenetically consistent, rank normalized and complete genome-based taxonomy. *Nucleic acids Res.* **50**, D785–D794 (2022).
111. Zhou, Z. et al. METABOLIC: high-throughput profiling of microbial genomes for functional traits, metabolism, biogeochemistry, and community-scale functional networks. *Microbiome* **10**, 33 (2022).
112. Helgeson, H. C., Kirkham, D. H. & Flowers, G. C. Theoretical prediction of the thermodynamic behavior of aqueous electrolytes by high pressures and temperatures; IV, Calculation of activity coefficients, osmotic coefficients, and apparent molal and standard and relative partial molal properties to 600 degrees C and 5kb. *Am. J. Sci.* **281**, 1249–1516 (1981).
113. Stefánsson, A. & Arnórsson, S. Gas pressures and redox reactions in geothermal fluids in Iceland. *Chem. Geol.* **190**, 251–271 (2002).
114. LaRowe, D. E. & Amend, J. P. Power limits for microbial life. *Front. Microbiol.* **6**, 718 (2015).

Acknowledgements

This research was supported by the Fondo Nacional de Desarrollo Científico y Tecnológico (FONDECYT) through grants 1171324, 1181773, 1201692, 1211515, and 1240245. Additional funding was provided by the Universidad Católica del Norte (UCN) through the Vicerrectoría de Investigación y Desarrollo Tecnológico (VRIDT), UCN-VRIDT Pro-Fondecyt "Mechanisms of adaptation of microbial communities of high-altitude geothermal environments and their importance for understanding the origin of life on early

Earth" and UCN-VRIDT2095 N°128/2022 "Bio-geochemical satellite recognition system in high-altitude hydrothermal ecosystems: climatic evolution and automated prediction models". P. Paquis was supported by an Agencia Nacional de Investigación y Desarrollo (ANID) doctoral scholarship (Folio N° 21221380), which also funded the dual doctoral program between UCN and Università degli Studi di Palermo (UNIPA). C. Pardo-Esté and J.Z. Florez were supported by ANID postdoctoral fellowships 3230189 and 3220102, respectively. We acknowledge Pedro and the Luca family for providing accommodation during field expeditions to Lirima, and Julio Ticuna for granting authorization to conduct research within the Lirima hydrothermal system. We thank Yasna Marambio Alfaro for her expertise in geochemical analyses, Felipe Docmac Monardes for assistance with stable isotopic studies, Ana María Zárate Riveira for fieldwork support, Lenka Kurte Palma for expedition organization and in-situ experimental analyses, and Jonathan García Araya for aerial drone imaging. This research benefited from collaborative arrangements with several institutional facilities at Universidad Católica del Norte, Chile: The Laboratorio de Ecología Molecular y Microbiología Aplicada (EMMA LAB), the Laboratorio de Geoquímica, the Centro de Investigación Tecnológica del Agua y Sustentabilidad en el Desierto (CEITSAZA), and the Unidad de Equipamiento Científico MAINI. We acknowledge scientific support from the Núcleo de Investigación No.7 UCN-VRIDT 076/2020, Núcleo de modelación y simulación científica (NMSC), for providing access to high-performance computing (HPC) facilities. We express gratitude to the Fish and Stable Isotope Ecology Laboratory and the University of Antofagasta Stable Isotope Facility (UASIF) at Universidad de Antofagasta, Chile, and to the Greenhouse Gas Laboratory (LABGEI) at Pontificia Universidad Católica de Valparaíso, Chile, for their collaborative contributions to this research.

Author contributions

Pablo Paquis: Conceptualization, Sample collection and analyses, Data curation, Formal analysis, Investigation, Methodology, Software, Validation, Visualization, Writing - original draft. Coral Pardo-Esté: Sample collection and analyses, Writing - review & editing. Joseline Tapia: Supervision, Writing - review & editing. July Z. Florez: Sample collection, Writing - review & editing. Vilma Pérez: Writing - review & editing. Verónica Molina: Sample collection, Writing - review & editing. Marcela Cornejo: Writing - review & editing. Pablo A. Pérez: Writing - review & editing. Chris Harrod: Writing - review & editing. Wade Jeffrey: Sample collection and analyses, Writing - review & editing. Sergio Calabrese: Writing - review & editing. Paola Quatrini: Writing - review & editing. Franco Tassi: Writing - review & editing. Martha B. Hengst: Conceptualization, Funding acquisition, Project administration, Resources, Supervision, Sample collection and analyses, Writing - review & editing.

Competing interests

The authors declare no competing interests.

Additional information

Supplementary information The online version contains supplementary material available at https://doi.org/10.1038/s43247-025-02817-w.

Correspondence and requests for materials should be addressed to Martha B. Hengst.

Peer review information *Communications Earth and Environment* thanks Kesava Priyan Ramasamy and Yongqin Liu for their contribution to the peer review of this work. Primary Handling Editors: [Nandita Basu]. A peer review file is available.

Reprints and permissions information is available at http://www.nature.com/reprints

Publisher's note Springer Nature remains neutral with regard to jurisdictional claims in published maps and institutional affiliations.

[1]Departamento de Ciencias Farmacéuticas, Facultad de Ciencias, Universidad Católica del Norte, Antofagasta, Chile. [2]Departamento de Ciencias Geológicas, Facultad de Ingeniería y Ciencias Geológicas, Universidad Católica del Norte, Antofagasta, Chile. [3]Dipartimento di Scienze della Terra e del Mare, Università degli Studi di Palermo, Palermo, Italy. [4]Instituto de Investigación en Riesgo Volcánico - CKELAR Volcanes, Antofagasta, Chile. [5]Núcleo Milenio en Turberas Andinas – AndesPeat, Arica, Chile. [6]Departamento de Ciencias y Geografía, Facultad de Ciencias Naturales y Exactas, y HUB Ambiental UPLA, Universidad de Playa Ancha, Valparaíso, Chile. [7]Australian Centre for Ancient DNA (ACAD), University of Adelaide, Adelaide, Australia. [8]Centre of Excellence for Australian Biodiversity and Heritage, University of Adelaide, Adelaide, Australia. [9]Center for Oceanographic Research COPAS COASTAL, Universidad de Concepción, Concepción, Chile. [10]Escuela de Ciencias del Mar, Facultad de Ciencias del Mar y Geografía, Pontificia Universidad Católica de Valparaíso, Valparaíso, Chile. [11]Instituto de Ciencias Naturales Alexander von Humboldt, Facultad de Ciencias del Mar y de Recursos Biológicos, Universidad de Antofagasta, Antofagasta, Chile. [12]Scottish Centre for Ecology and the Natural Environment, School of Biodiversity, One Health and Veterinary Medicine, University of Glasgow, Glasgow, UK. [13]Center for Environmental Diagnostics and Bioremediation, University of West Florida, Pensacola, FL, USA. [14]Istituto di Geofisica e Vulcanologia (INGV), sez Palermo, Palermo, Italy. [15]Department of Earth Sciences, University of Florence, Florence, Italy. [16]Institute of Geosciences and Earth Resources (IGG), National Research Council of Italy (CNR), Florence, Italy. ✉e-mail: mhengst@ucn.cl